Neotectonics of the Min Shan, China: Implications for mechanisms driving Quaternary deformation along the eastern margin of the Tibetan Plateau

Eric Kirby*
Kelin X. Whipple
B. Clark Burchfiel
Dpartment of Earth, Atmospheric, and Planetary Sciences, Massachusetts Institute of Technology, Cambridge, Massachusetts 02139

Wenqing Tang
Chengdu Institute of Geology and Mineral Resources, Chengdu, Sichuan Province, China

Glenn Berger
Desert Research Institute, 2215 Raggio Parkway, Reno, Nevada 89512

Zhiming Sun
Zhiliang Chen
Chengdu Institute of Geology and Mineral Resources, Chengdu, Sichuan Province, China

ABSTRACT

The Min Shan region, located along the eastern margin of the Tibetan Plateau north of the Sichuan Basin, provides an important natural laboratory in which to study the rates and patterns of deformation and their relationship to mountain building at the margin of the plateau. The topographic margin of the plateau is coincident with a north-trending mountain range, the Min Shan, that stands nearly 2 km above the mean elevation of the plateau (~3500 m in this region). We exploit the preservation of a series of variably deformed Quaternary sediments along the western flank of the range to investigate the Pleistocene-Holocene deformation field within the Min Shan region. Mapping and field observations of remnant alluvial fans of late Pleistocene age indicate that deformation within the Min Shan involved substantial (~10°), rapid, down-to-the-northwest tilting. The geometry of the deposits and the partial preservation of an erosion surface beneath the basin suggest that much of the modern relief of the Min Shan relative to the Tibetan Plateau is a consequence of this late Pleistocene tilting. Rates of tilting inferred from luminescence dating of interbedded loess have been remarkably rapid (~10^{-8} rad/yr). Similarly rapid rates of Holocene differential rock uplift are inferred from tilted lacustrine sediments in the southwestern part of the range. The range is bounded on the west by the Min Jiang fault zone, an east-vergent reverse fault. However, Holocene alluvial terraces in headwaters of the Min River are preserved across the fault in several places, indicating that displacement rates on the Min Jiang fault are <1 mm/yr. Active faulting only occurs along the eastern foot of the range (Huya fault) for a short distance (~60 km), despite 3 km of relief on the eastern range front. The relationship between these structures and the tilting observed in the Min Jiang basin is enigmatic; the faults do not appear to exert a strong control on the rates and pattern of deformation within the basin. A simple flexural model demonstrates that rates of tilting on the western flank of the Min Shan are too high to be simply attributed to an isostatic response to surficial loading and unloading of the lithosphere. Present-day horizontal shortening across the Min Shan is geodetically determined to be less than 2–3 mm/yr, suggesting that only a small part of the observed tilting can be attributed to horizontal shortening. Thus, tilting and concomitant differential rock uplift in the Min Shan appear to require an additional driving component. We suggest that Quaternary deformation along the western Min Shan may reflect the surface response to thickening of a weak lower crust at the margin of the Tibetan Plateau.

Keywords: neotectonics, Tibetan Plateau, mountain building, flexure, Sichuan Basin, lower crust.

INTRODUCTION

Since the recognition that widespread intracontinental deformation within central Asia is the result of the Cenozoic collision of India and Eurasia (Argand, 1924; Molnar and Tapponnier, 1975), there has been a long-standing debate centered on the degree to which crustal thickening within the Tibetan Plateau accommodates convergence between the two continents (cf. England and Houseman, 1986; Tapponnier et al., 1982). Although most workers agree that the present crustal thickness of nearly 70 km and the great elevation (Fielding et al., 1994) of the plateau are the result of the collision (Dewey and Burke, 1973; Harrison et al., 1992; Molnar, 1988), the amount, rates, and style of shortening within Tibet as well as its spatial and temporal distribution remain largely unknown (Burchfiel and Royden, 1991; Coward et al., 1988). Many of the models for Asian deformation predict markedly different kinematics in the region east and northeast of the Indian indenter (Avouac and Tapponnier, 1993; Cobbold and Davy, 1988; England and Molnar, 1990b); thus, one means of distinguishing between competing models is to determine the kinematics of deformation within this region of the plateau. Our first goal therefore is to document the distribution and rates of late Cenozoic deformation in the north-trending mountain range termed the Min Shan—a little-known but important segment of the eastern margin of the Tibetan Plateau north of the Sichuan Basin, in Sichuan Province, China.

Our second goal is to evaluate the processes driving deformation at the margin of the plateau. Along much of the eastern margin there is a lack of correlation between the surface expression of structures and topography (Burchfiel et al., 1995; Royden et al., 1997). Faults and folds are often oblique to, and commonly older than, the topographic margin. These observations—coupled with satellite geodesy (King et al., 1997; Chen et al., 2000) and increasing evidence for a weak lower crust beneath Tibet (Jin et al., 1994; Nelson et al., 1996; Masek et al., 1994a)—led Royden et al. (1997) to suggest that crustal thickening in eastern Tibet may be focused in the lower crust. In this model, rock and surface uplift may be due

*E-mail: ekirby@mit.edu.

GSA Bulletin; March 2000; v. 112; no. 3; p. 375–393; 11 figures; 3 tables.

to isostatic and dynamic responses to lower-crustal thickening and not directly related to horizontal shortening of the upper crust. Our mapping and field observations along the Min Shan suggest that it is difficult to account for the pattern of surface deformation inferred from tilted Quaternary sediments by displacement on recognized structures. Furthermore, rates of late Pleistocene tilting along the western flank of the range far exceed geodetically measured rates of horizontal shortening (King et al., 1997; Chen et al., 2000). Thus, our results suggest the presence of an additional driving force and are permissive of thickening driven by lower-crustal flow.

Our third goal, intimately linked to the other two goals, is to evaluate the morphologic evolution of the Min Shan and, in particular, to ascertain to what degree high mountain ranges along the eastern margin of the plateau may reflect an isostatic response to erosion at the margin. Topographically high mountain ranges commonly occur at the edges of continental plateaus (Fielding et al., 1994) and may be (1) primarily tectonic features related to the dynamics of shortening at the margin (Lyon-Caen and Molnar, 1983; Royden et al., 1997), (2) primarily isostatic features related to mass removal along the topographic front (Masek et al., 1994b; Molnar and England, 1990; Montgomery, 1994) or, (3) some combination of both mechanisms (Burbank, 1992). The lack of large-magnitude shortening across the eastern margin (Burchfiel et al., 1995) makes this an important region in which to test the hypothesis of isostatically generated topography. In this paper, we argue from a simple flexural model that the rates of observed surface deformation in the Min Shan require unreasonably high rates of mass removal by erosion to produce the topography isostatically and thus point to the importance of additional driving mechanisms.

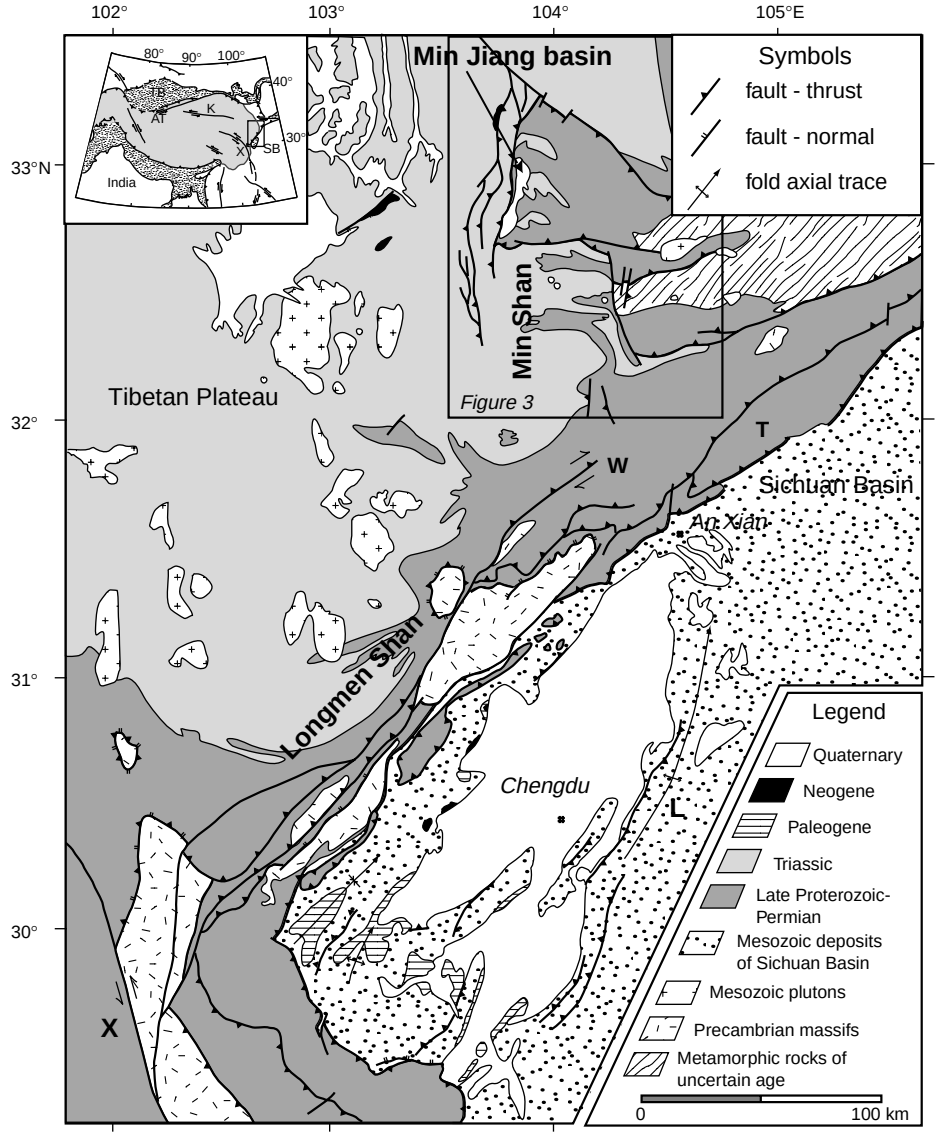

Figure 1. Simplified geologic map of the Longmen Shan region of the eastern Tibetan Plateau. Geology modified after Burchfiel et al. (1995), 1:200 000 geologic maps (Ministry of Geology and Mineral Resources, People's Republic of China, 1991), and our mapping. Inset shows location of the region relative to major tectonic elements of the Indo-Asian collision zone. Abbreviations: AT—Altyn Tagh fault, K—Kunlun fault, L—Longquan anticline, T—Tangwangzhai nappe, TB—Tarim basin, SB—Sichuan Basin, W—Wenchuan-Maowen fault zone, X—Xianshuihe fault.

BACKGROUND

In this section we summarize the salient parts of the late Cenozoic tectonics along the eastern margin of the Tibetan Plateau to set the background for our work in the Min Shan region. We follow Burchfiel et al. (1995) in using the term "Longmen Shan region" to refer to the eastern margin of the Tibetan Plateau along the edge of the Sichuan Basin between the Xianshuihe fault and the west Qinling Shan, and we use the term "Min Shan region" to refer to the margin of the plateau north of the Sichuan Basin (Fig. 1).

Active Tectonics of the Longmen Shan

The topographic margin of the Tibetan Plateau along the Longmen Shan is one of the most impressive continental escarpments in the world; from the Sichuan Basin at 500 to 700 m elevation, the land rises westward to peak elevations exceeding 6000 m over horizontal distances of 40–60 km. This topographic front led a number of workers to suggest that it was the locus of major active shortening (up to 20 mm/yr) between Tibet and south China (Avouac and Tapponnier, 1993; Ratschbacher et al., 1996). Recent results of GPS (Global Positioning System) space geodetic surveys indicate, however, that modern shortening rates across this margin must be less than 2–3 mm/yr and are within uncertainty of zero (King et al., 1997; Chen et al., 2000). Seismicity along this margin is generally restricted to small events ($M < 5$) that occur in a band paralleling the topographic margin (Editorial Board, State Seismological Bureau, 1989). The historic record of earthquakes in this region extends back over 1500 yr and documents a remarkable lack of significant ($M > 4–5$) events (Editorial Board, State Seismological Bureau, 1989), consistent with the slow shortening rates inferred from GPS.

Geologic evidence for active faulting in the northern Longmen Shan is equally scant and appears to be restricted to the Min Shan region (Burchfiel et al., 1995; Chen et al., 1994). Thrust

faults along the topographic front in the northern Longmen Shan (northeast of An Xian along the Tangwangzhai nappe; Fig. 1) are overlapped by Upper Triassic terrestrial clastic rocks, restricting the latest displacement along these faults to Mesozoic time (Burchfiel et al., 1995).

The absence of significant late Cenozoic shortening across the Longmen Shan is corroborated by a distinct lack of foreland sedimentation. Cenozoic deposits are restricted to the southwestern corner of the Sichuan Basin (Fig. 1) and are generally <500 m in thickness. Quaternary sediments in particular consist of a thin (<100 m) veneer in this region and appear to be ponded behind the Longquan anticline (Fig. 1). Although this anticline may be active, definitive evidence is lacking (Burchfiel et al., 1995). Elsewhere throughout the Sichuan Basin, modern sediments are routed to the East China Sea via tributaries of the Yangtze River. Thus, the Sichuan Basin does not appear to have been flexurally loaded during the Cenozoic (Royden et al., 1997). Indeed, in the northwestern corner of the basin (northeast of An Xian, Fig. 1), hogbacks of Mesozoic red beds ramp up toward the plateau, suggesting that the basin may have been flexurally upwarped during the late Cenozoic.

The slow modern velocity field, the lack of a Cenozoic foredeep, and the limited Cenozoic shortening across the Longmen Shan led Royden et al. (1997) to hypothesize that much of the development of this region of the plateau may be the result of eastward flow of weak lower crust from beneath the central plateau. Where this material impinges on the strong crust of the Sichuan Basin, it may focus crustal thickening (and consequent surface uplift) in the absence of significant upper-crustal shortening.

Tectonic Setting of the Min Shan

The Min Shan is a topographically high-standing mountain range that delineates the edge of the Tibetan Plateau for nearly 200 km north of the Sichuan Basin (Figs. 1 and 2A). The range is 40–50 km wide and contains peaks that reach elevations of 5600 m. The mean elevation of the plateau in this region is ~3500 m, and relief on the western flank of the range approaches 2 km (Fig. 2B). Although regional topographic gradients across this margin of the plateau are not as large as along the Sichuan Basin, the eastern flank of the Min Shan drops 3–4 km to the lowlands of the west Qinling orogen (<1000 m) over a lateral distance of 60–80 km.

Despite the impressive mountain front along the eastern Min Shan, active faults occur only along the central 60 km of the range front. Here the Huya fault juxtaposes Devonian–Triassic siliciclastic and carbonate rocks on the west with Proterozoic crystalline basement and cover sequences of the west Qinling orogen to the east (Fig. 3). The fault strikes just west of north and dips steeply (70°–85°) to the west. A series of earthquakes along the fault in 1976 demonstrate that active displacement across the fault is oblique reverse motion with a left-lateral component (Han and Xia, 1980; Jones et al., 1984). Hypocentral locations for these shocks are not well determined, but appear to be between 10 and 15 km deep (Jones et al., 1984), suggesting that the fault remains steep throughout much of the upper crust (Fig. 3).

The Min Shan is bounded along much of its western flank by another reverse fault, the Min Jiang fault zone. The Min Jiang fault zone consists of several strands of high-angle faults (Burchfiel et al., 1995; Chen et al., 1994), the easternmost of which is hereafter referred to as the Min Jiang fault. The Min Jiang fault cuts Quaternary deposits along the headwater reaches of the Min Jiang (jiang = river) and is clearly a recently active structure (Burchfiel et al., 1995; Chen et al., 1994; Tang et al., 1993; Zhao et al., 1994). However, geologic estimates of the magnitude, rates, and sense of displacement vary widely in the literature (cf. Chen et al., 1994; Zhao et al., 1994). Consequently, the significance of the Min Jiang fault in the active deformation field at the edge of the plateau is unknown.

Despite the presence of active faults on either flank of the Min Shan, recent geodetic surveys in the northern Longmen Shan region demonstrate that, within uncertainties of ~2–3 mm/yr, there is no active shortening across the range (King et al., 1997; Chen et al., 2000) (Fig. 2). However, as both the Min Jiang and Huya faults have steep (>60°) westward dips, horizontal shortening associated with active reverse faulting may be minor. It is important to note, however, that the geodetic data restrict any vertical component of deformation associated with shortening across the Min Shan to less than a few millimeters per year. With the exception of the 1976 earthquake sequence on the Huya fault, historic seismicity along the eastern Min Shan appears to be limited to one large (approximate magnitude of 7–8) event in 1879 (Editorial Board, State Seismological Bureau, 1989). Thus, the geodetic measurements are likely representative of the regional velocity field over the past 1000–2000 yr and are consistent with slow horizontal strain accumulation across the range.

Neogene–Quaternary deposits are preserved along the western flank of the Min Shan in the headwaters of the Min Jiang (hereafter referred to as the Min Jiang basin—Figs. 1 and 3). They represent one of the only significant exposures of upper Cenozoic sediment preserved in this region of the Tibetan Plateau. We mapped these deposits and their structural relationships at a scale of 1:100 000 over the course of three field seasons between 1996 and 1998 (Fig. 4). Because the older sediments are progressively more deformed, we are able to place constraints on the displacement across the Min Jiang fault, as well as to evaluate the late Cenozoic deformation field within the Min Shan range itself.

STRATIGRAPHY OF THE MIN JIANG BASIN

Pre-Cenozoic Rocks of the Min Shan

Paleozoic–Mesozoic rocks in the Min Shan region comprise a thick (>4000 m) section of platformal, shallow-water siliciclastic rocks and reef-bearing limestones. We follow Burchfiel et al. (1995) in referring to this region as the Xue Shan platform. In the northern Min Shan, the platformal rocks are continuous to the east with late Proterozoic–Silurian rocks that rest unconformably on metamorphic rocks shown as Precambrian on published Chinese geologic maps (Fig. 3). However, to the west of the Min Jiang fault zone, Carboniferous and Permian rocks thin to nearly half their thickness on the platform. The overlying Triassic rocks change from shallow-water limestones to thick deposits of deep-water flysch characteristic of the Songpan-Garze basin. Thus, the Min Jiang fault zone marked an important paleogeographic boundary in the Paleozoic and early Mesozoic and may have been a structural boundary at this time (Burchfiel et al., 1995).

Pliocene Deposits

The oldest Cenozoic deposits in the study area are a series of small, discontinuous lenses of Tertiary conglomerates. The deposits are restricted to elongate exposures preserved along strands of the Min Jiang fault system (Tp; Figs. 2, 4) and are mapped as late Neogene (Pliocene) on Chinese geologic maps (Ministry of Geology and Mineral Resources, People's Republic of China, 1991). Near Kakagou (Fig. 4), well-indurated, coarse conglomerate is faulted against Triassic limestone. The conglomerate is weathered to a deep red color that is suggestive of its relative antiquity. However, the absolute age of these deposits is unknown, owing to the lack of datable material and/or fossils. Likewise, the original extent of these deposits cannot be confidently reconstructed. Their present geometry along the Min Jiang fault system, however, implies that they may have been restricted basins ponded during initiation of the fault system (Chen et al., 1994).

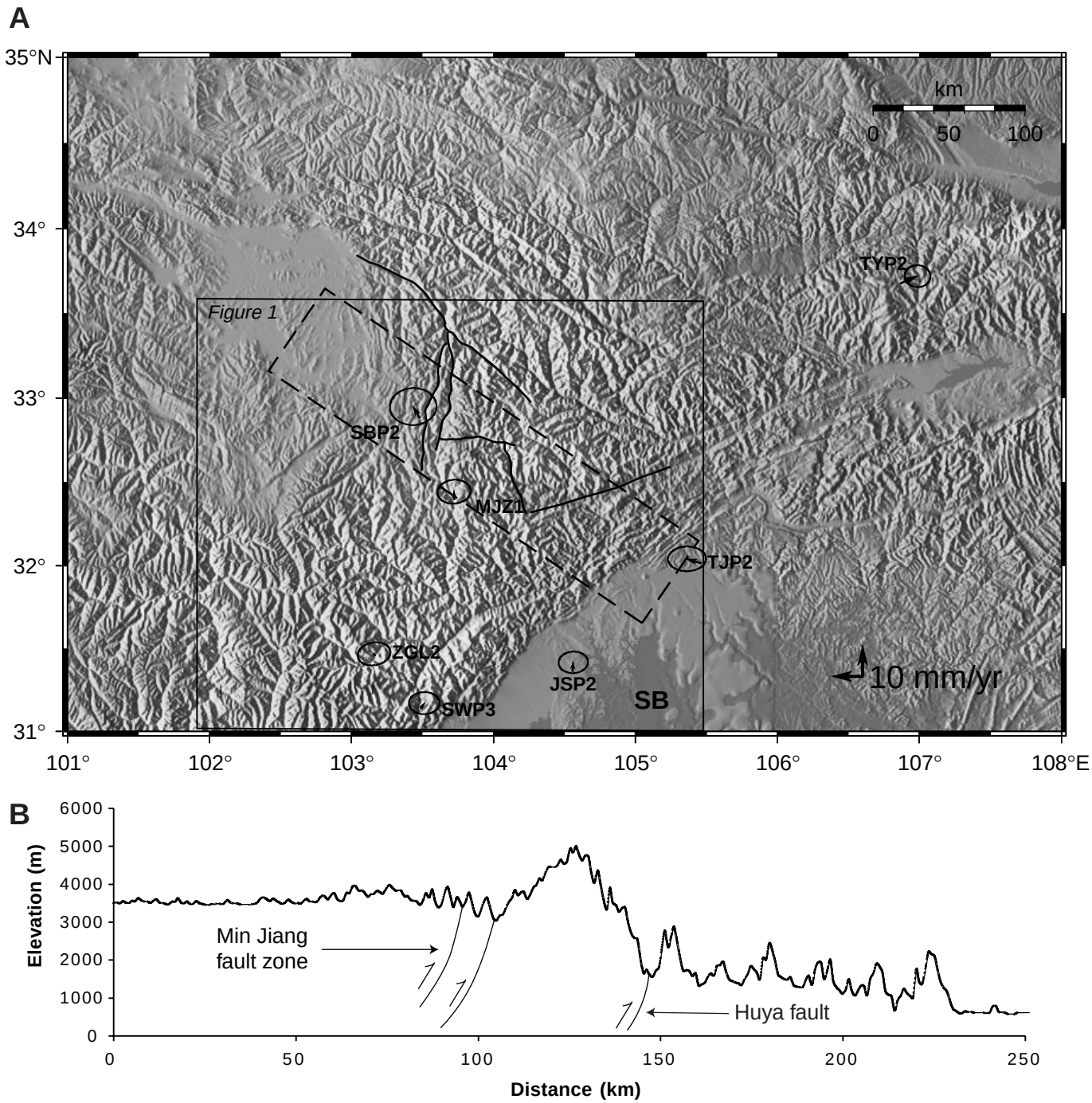

Figure 2. (A) Regional topography (GTOPO30; nominal resolution 1 km) and GPS velocities of the northern Longmen Shan region (Chen et al., 2000). Station names and coordinates can be found in King et al. (1997). Uncertainty ellipses are plotted at 95% confidence intervals. Major structures in the Min Shan are shown for reference to Figure 1 (box). SB—Sichuan Basin. Dashed rectangle shows region of topography used in flexural model (Fig. 10). (B) Schematic cross section depicting position of the Min Shan at the margin of the Tibetan Plateau and its relationship to the Min Jiang and Huya faults. Topography taken from a single profile near the northwest-southeast centerline of the dashed rectangle in A.

Quaternary Deposits

Quaternary deposits in the Min Jiang basin can be subdivided into two broad categories: middle Pleistocene–upper Pleistocene alluvial conglomerates and upper Pleistocene–Holocene alluvium related to the current Min Jiang drainage (Figs. 4 and 5). We designate relative ages with subscripts ranging from 1 to 4 (oldest to youngest). We caution, however, that these relative-age designations are restricted to this basin and should not be confused with similarly designated deposits elsewhere in China (similar labels are commonly used to represent absolute age on Chinese geologic maps) (Ministry of Geology and Mineral Resources, People's Republic of China, 1991).

Middle Pleistocene conglomerates (Q_1 in Fig. 4) form most of the deposits within the Min

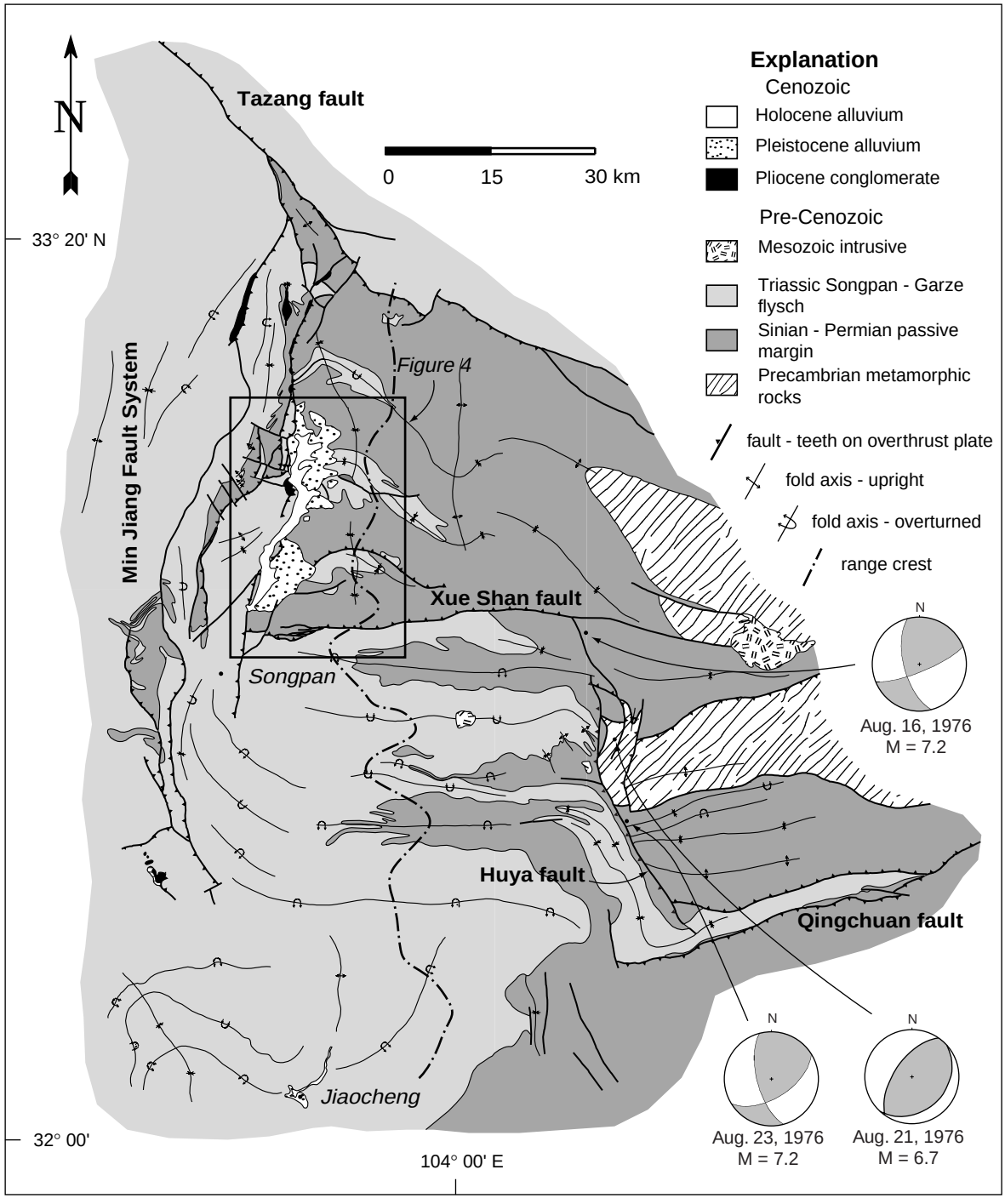

Figure 3. Geologic map of the Min Shan and surrounding region depicting major structures bounding the Min Shan and their relationship to Quaternary sediments in the Min Jiang basin. Dash-dot line represents the approximate trace of the high topography along the range crest. Epicenters and focal mechanisms of the 1976 Songpan earthquake swarm adapted from Jones et al. (1984). Map was compiled from 1:200 000 geologic maps (Ministry of Geology and Mineral Resources, People's Republic of China, 1991) and our work. Location of Figure 4 shown in box.

Jiang basin (Guanyin Shan Formation) (Chen et al., 1994). Q_1 deposits are bounded on the west by the Min Jiang fault. They are composed of a series of west-dipping coarse-gravel and boulder conglomerates, interbedded near their base with 10–20 cm beds of fine sand, silt, and reworked loess. Q_1 deposits are locally well indurated and are often exposed in 10–30 m high cliffs. Clasts within the Q_1 conglomerates range from 5 to 30 cm in diameter and are well rounded and well sorted. Clast composition is primarily limestone (>90%), with minor sandstone and siltstone material. The conglomerates are clast supported and contain a weak to moderate crystalline calcareous cement.

Figure 4. Geologic map of the Min Jiang basin depicting the relationships between the Min Jiang fault and Quaternary sedimentary deposits along the west flank of the Min Shan. Note the lack of faults east of the basin proper. Topographic base was originally 1:100 000. Inset is an equal-area, lower-hemisphere projection of poles to bedding in Q_1 conglomerate showing its uniform west-northwest dip.

Q_1 conglomerates were deposited on a bedrock surface of low relief in westward-thickening wedges. Maximum preserved thickness reconstructed from the mapped geometries is nearly 200 m at the western margin of the deposits. Clast compositions are similar to Mississippian–Permian limestones exposed in the Min Shan and distinct from the turbiditic flysch of the Triassic to the west (Chen et al., 1994). Clast imbrication within the deposits indicates a component of west-directed transport during deposition. The alluvial character of the deposits, their geometry, clast composition, and transport directions all suggest that Q_1 conglomerates were derived from the Min Shan range, and we interpret them as remnant alluvial fans draped along the west flank of the range.

These alluvial fans are now dipping west between 12° and 16° (Figs. 4 and 6A) and have been deeply eroded by the modern streams draining the Min Shan. In the northern end of the basin, near the town of Gonganin, Q_1 alluvial fans are deeply dissected into high remnant hills and mesas (Fig. 6B). Streams draining this part of the Min Shan have incised through the Q_1 and 40–80 m into the underlying Paleozoic carbonates. Thus, total incision along tributaries to the Min Jiang exceeds 200 m since abandonment of the alluvial fans. The conglomerates were deposited on a bedrock surface that currently dips west at a slightly steeper angle than the Q_1 beds (15°–18°) and is preserved along ridge crests east of the mapped extent of Q_1 deposits (Figs. 4 and 6C). The age of this unconformity is unknown.

Q_1 conglomerates are overlain at one locality east of Zhangla (Fig. 4) by 10 m of slightly less indurated gravel. The gravels are separated by a 1–2-m-thick loess bed and have a slight (2°–5°) angular discordance across this bed. The loess has a well-developed reddish weathering profile that extends into the upper 1 m of the Q_1 conglomerates beneath it. Small 0.5–1 cm clay nodules occur at the contact of the loess and the Q_1 conglomerates. We interpret the gravels above this horizon to be a younger, but related, deposit that we have mapped as $Q_{1–2}$. The angular unconformity and paleosol indicate that this horizon marks an important local hiatus in deposition. Bedding in the $Q_{1–2}$ gravels above the unconformity locally dips moderately to the east (Fig. 4), similar to the Q_1 gravels below. Both units are folded on the western limb of an open syncline (Fig. 4) and thus predate much of the folding.

Other deposits of probable $Q_{1–2}$ age are preserved throughout the southern and western parts of the Min Jiang basin. The deposits are generally moderately well indurated gravels, which are slightly reddish in color with a clay-rich matrix. We correlate them with the $Q_{1–2}$ east of Zhangla primarily on the character of the deposit and the degree of induration. We recognize the uncertainties in such a correlation, but rely on it in the absence of material available for absolute dating. It is possible that deposits mapped as $Q_{1–2}$ span a relatively large time between the deposition of Q_1 and alluvial terraces of Q_2 age.

$Q_{1–2}$ deposits are also exposed immediately beneath the Min Jiang fault along the southwestern edge of the Min Jiang basin, west of the town of Zhangla (Fig. 4). They consist of two types of intercalated deposits: rounded alluvial gravels similar to those described above and angular breccias set in a red clay matrix. The gravels strike to the northwest and dip northeast. The breccias typically consist of clasts similar to the Triassic limestone west of the Min Jiang fault. They are interpreted as colluvial material shed off the hanging wall of the fault. The presence of locally derived talus within these deposits suggests that the former western margin of the basin was near its present-day position. A thin veneer of loess and colluvium (Fig. 4) covers $Q_{1–2}$ deposits throughout most of the southern Min Jiang basin.

Similar alluvial deposits crop out over a wide region in the northwest corner of the Min Jiang basin (west of Gonganin, Fig. 4). Gravels here are moderately well indurated and consist of 10–20 cm cobbles set in a reddish clay matrix. They are interfingered with breccia deposits similar to those exposed in the southwest. Exposure in this part of the basin is generally poor, but where we find exposures of the gravels, they dip moderately to steeply west and are locally folded beneath the Min Jiang fault.

Late Quaternary Alluvial Terraces

Fluvial terraces preserved along the Min Jiang from the headwater region near Gonganin to the town of Songpan (Fig. 2) consist of deposits of late Pleistocene–Holocene age. Between Gonganin and Chuanjiusu, two levels of fill terraces are inset into the older Pleistocene deposits (Chen et al., 1994). The higher terrace (Q_2) is preserved in discontinuous exposures only within the Min Jiang basin, whereas the lower terrace (Q_3) is continuous between the headwater regions and the town of Songpan.

The Q_2 terrace consists of ~40 m of gravel and is best exposed in the northern part of the basin. In this region, Q_2 gravels have only a moderately well developed weathering horizon with a clay-rich matrix confined to the upper 1 m of the deposit. Terrace surfaces preserved along the eastern bank of the Min Jiang dip 2°–3°W and appear to represent tributary fans draining into the Min Jiang. Elsewhere in the northern basin, terrace surfaces are not preserved, but discontinuous exposures of similar alluvium suggest that they were once present along much of the river (Fig. 4).

The Q_2 terrace is also exposed along the western side of the Min Jiang in the southern part of the basin (Fig. 4). Here it consists of ~30 m of alluvial gravel and has a colluvial wedge composed primarily of reworked loess draped atop it. The colluvial wedge contains rare boulders of Triassic limestone and of older Pleistocene conglomerate. The terrace is cut by the Min Jiang fault west of the town of Zhangla and provides an important relative timing constraint on the youngest displacement along the fault (discussed subsequently).

The Q_3 terrace along the Min Jiang is continuous between Gonganin and Songpan (Fig. 4). Within the Min Jiang basin, the terrace consists of 15–35 m of coarse-gravel fill inset into the older deposits (Fig. 6A). The terrace has no appreciable soil development and is overlain by alluvial fans whose sources were the main tributaries in the basin. In the center of the basin, this terrace is locally a strath bench inset into a large landslide that fills much of the valley near the Gamet monastery (Fig. 4). The Q_3 terrace locally onlaps the Min Jiang fault and thus places an upper bound on the timing of displacement across the fault (discussed subsequently).

Despite the continuity of the Q_3 terrace across the southern margin of the Min Jiang basin, the nature of the terrace changes south of Chuanjiusu. Terraces within the Min Jiang basin are entirely alluvial fill, whereas south of the basin margin, the Q_3 terrace is a strath terrace whose tread ranges from 5 to 10 m above the modern channel. The Q_3 terrace along this reach generally has a cap of alluvial gravels that ranges from 5 to 15 m in thickness and is overlain by tributary alluvial fans. South of Songpan, the terrace is not present, but tributary alluvial fans are ubiquitous, and their distal parts are generally truncated by recent incision of the Min Jiang. These fans are probably contemporaneous with alluvial fans preserved atop the Q_3 terrace.

Modern alluvium is confined to the bed of the Min Jiang and its tributaries, consists of gravel- to boulder-sized clasts of carbonate, and is mapped as Q_4 (Fig. 4).

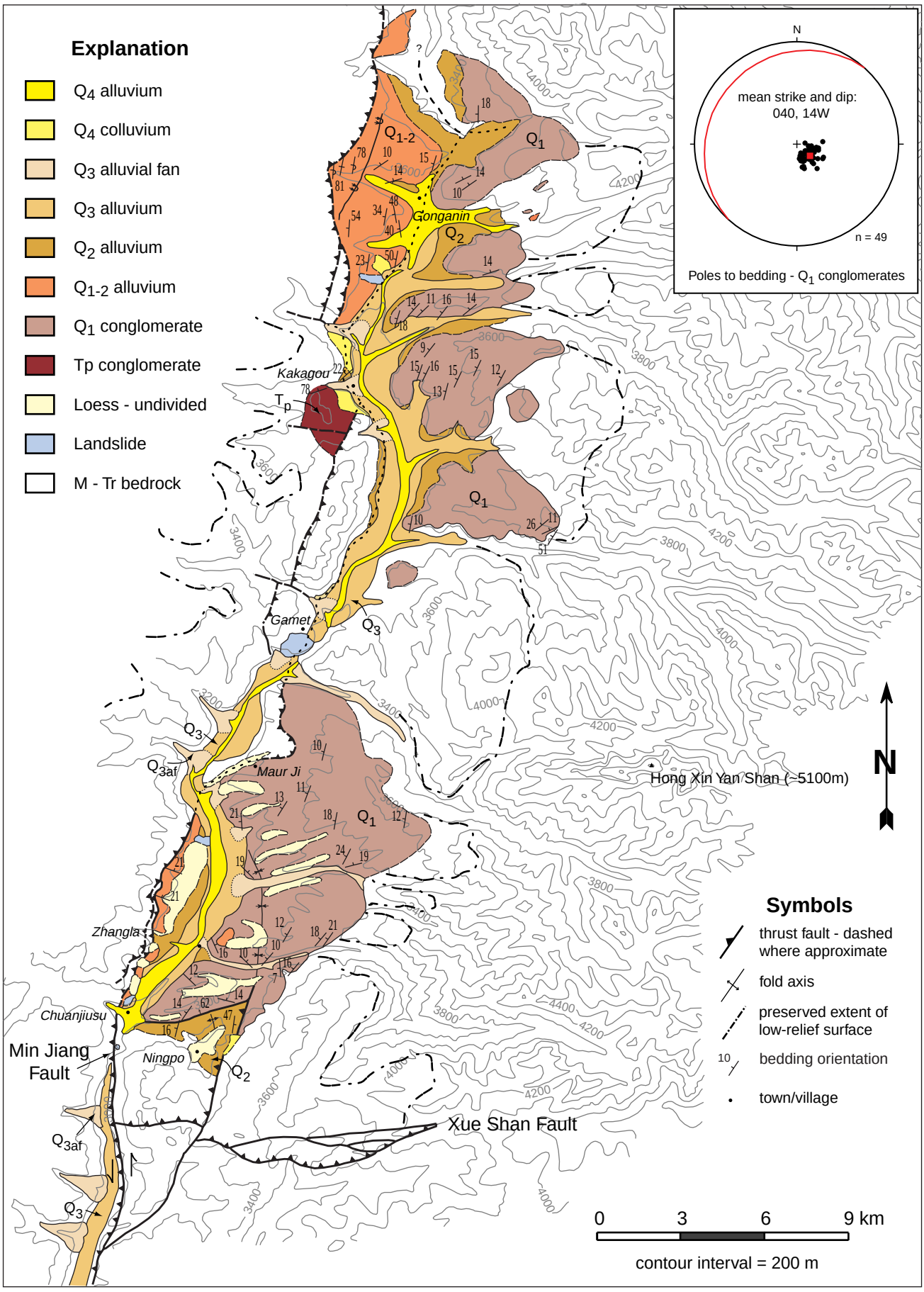
Explanation
Q4 alluvium
Q4 colluvium
Q3 alluvial fan
Q3 alluvium
Q2 alluvium
Q1-2 alluvium
Q1 conglomerate
Tp conglomerate
Loess - undivided
Landslide
M - Tr bedrock
N
mean strike and dip:
040, 14W
n = 49
Poles to bedding - Q1 conglomerates
Gonganin
Kakagou
Gamet
Maur Ji
Zhangla
Chuanjiusu
Ningpo
Min Jiang Fault
Xue Shan Fault
Hong Xin Yan Shan (~5100m)
Symbols
thrust fault - dashed where approximate
fold axis
preserved extent of low-relief surface
bedding orientation
town/village
0 3 6 9 km
contour interval = 200 m

CHRONOLOGY OF THE MIN JIANG BASIN DEPOSITS

In order to assess the absolute age of the deposits within the Min Jiang basin we collected samples for ^{14}C and photon-stimulated luminescence (PSL) dating. The latter technique can be a sensitive means for dating the burial time of detrital grains of sediment (e.g., Aitken, 1998). The particular approach employed here (IRSL, or infrared-stimulated luminescence) produces a signal from fine, silt-sized feldspars. The technique relies on an assumption that the natural luminescence of detrital grains was zeroed by exposure to sunlight prior to final deposition. Although the insolation histories are unknown, we selected samples from facies most likely to represent depositional settings favorable to luminescence resetting (e.g., eolian silt, laminated lacustrine silt). Furthermore, the IRSL method is extremely sensitive to daylight; as little as a few minutes insolation can remove >90% of the IRSL signature (Aitken, 1998). IRSL sampling and analytical techniques are presented in the Appendix.

^{14}C Chronology: Q_2 and Q_3 Terraces

Detrital charcoal from fine-sand beds near the top of the Q_3 terrace north of Zhangla (Fig. 4) provides age constraints for the timing of displacement on the Min Jiang fault. Analytical data and ages are reported in Table 1. Sample EK 97-9 (angular fragment of charcoal 1–2 cm in diameter) was collected from a fine-sand layer interbedded with gravel ~1 m below the surface of the Q_3 terrace and gave a calibrated age of 8129–8420 yr B.P. (2σ). Sample EK 97–8 (multiple detrital charcoal fragments <1 mm in diameter) was collected from a similar sandy lens within the terrace gravels (~0.5 km south of 97–9) and yielded an age of 6670–6944 yr B.P. (2σ). We also collected a single sample of charcoal-rich soil (EK 97–10) from a fine-grained alluvial fan atop the terrace at Zhangla (Fig. 4). Conventional ^{14}C analysis on the bulk organic fraction gave an average age of 2742–2993 yr B.P. (2σ) that places a minimum bound on the age of the terrace. We obtained a fourth sample (EK 97–26) of wood from within a colluvial and landslide deposit draped atop the Q_3 terrace just west of the town of Chuanjiusu (Fig. 4). This sample yielded a conventional ^{14}C age of 14 118–15 720 yr B.P. (2σ), suggesting that some of the Q_3 terrace gravels were deposited in the latest Pleistocene. Although it is possible that this wood may be recycled to some degree, we find it unlikely that woody material would remain intact for many thousands of years at the surface, and we interpret this age as the approximate time of burial of wood within the slide deposit. Taken as a whole, ^{14}C chronology suggests that the Q_3 terrace gravels range in age from >14 000 yr to 6600 yr B.P.

TABLE 1. RADIOCARBON ANALYSES OF CHARCOAL SAMPLES

Sample number	Stratigraphic unit	$\delta^{13}C$ (‰)	^{14}C age (yr B.P. ± 1σ)	^{14}C age (corrected)* (yr B.P. ± 1σ)	Calendric age range (yr B.P. ± 2σ)
EK 97-10†	Q_4 fan	–25.7	2730 ± 75	2810 ± 77	2742–2993
EK 97-8§	Q_3 terrace	–23.4	5945 ± 55	6120 ± 57	6670–6944
EK 97-9§	Q_3 terrace	–12.5	7525 ± 55	7750 ± 57	8129–8420
EK 97-26†	Q_3 colluvium	–22.1	12560 ± 180	12940 ± 185	14118–15720
EK 96-1§	Q_2 alluvium	–25.9	22780 ± 340	23460 ± 350	N.D.

Note: Samples are listed in stratigraphic order (see Fig. 5 for relative stratigraphic sample locations). Reported ^{14}C ages use Libby's half life (5568 yr) and are referenced to the year A.D. 1950. Analytical uncertainties are 1σ and reflect the total uncertainty in the measurement. Calendric ages calibrated using the University of Washington CALIB program (Stuiver and Reimer, 1993). N.D.—not determined.

*The corrected age is the due to the 3% difference between the Libby half life of ^{14}C (5568 yr) and the actual half life (5735 yr).

†Conventional ^{14}C measurement performed at Geochron Laboratories, Cambridge, Massachusetts. Sample 97-10 consists of a charcoal-rich organic soil horizon. The clay/organic fraction was isolated by ultrasound dispersion, filtered to remove rootlets, and treated with dilute HCl to remove carbonate. Sample 97-26 consists of wood. It was washed, split into small pieces, treated with HCl to remove carbonate, and with NaOH to remove humic acids.

§AMS measurement performed by G. Burr at the University of Arizona AMS facility.

Although we were unable to obtain datable material from the Q_2 terrace proper, relationships with alluvial sediments of late Pleistocene age near Ningpo (Fig. 4) suggest that the terraces probably date to the late Pleistocene. We obtained detrital charcoal fragments from east-dipping sands and silts north of the town of Ningpo (Fig. 4). The sediments interfinger with coarse gravels near the modern Min Jiang, and we interpret them as fine-grained alluvial-fan deposits transitional with Q_2 fluvial terraces. Although this correlation is somewhat tentative, the unconsolidated nature of the sediments and the presence of a thin (<5 m) loess cap are consistent with relationships observed on well-preserved Q_2 terraces along the western side of the Min Jiang. Sample EK 96-1 yielded a ^{14}C age of 22 780 ± 340 yr B.P. (1σ), which implies that Q_2 deposits date to the late Pleistocene.

IRSL Chronology: Q_1 Deposits

We also collected three samples for luminescence dating (IRSL method). Two of these samples were collected from loess and silt interbedded with the Q_1 conglomerates and place important bounds on the age of these deposits. A third sample, collected from young lacustrine sediments along the Min Jiang (north of Jiaocheng; Fig. 3), allowed us to test the IRSL multi-aliquot zeroing assumption. This assumption states that all grains were exposed to daylight for more than tens of minutes prior to final deposition. Analytical techniques for all three samples are presented in the Appendix, dosimetry data are presented in Table 2, and luminescence data are presented in Table 3.

All IRSL experiments employed a two-temperature preheating protocol (Table 3). Separate batches of aliquots (discs, each having ~0.5 mg of grains on an Al substrate) were given different heat treatments as reported in Table 3. The rationale for this protocol is that statistical agreement of the paired equivalent dose (D_E) values is expected to indicate that a thermally stable IRSL signature has been isolated. In this case, the weighted mean D_E value is used in the age calculation (Table 3).

Examples of the IRSL data are shown in Figure 7. Dose-response curves (center) illustrate the reproducibility of individual data points (one for each aliquot). The IRSL signatures (after preheating) for all samples were not large and evinced relatively large scatter. For sample TIBT 98-2 (EK 98-5) and the 170 °C experiment of sample TIBT 98-4 (EK 98-9), short-shine normalization (Ollerhead et al., 1994) did not reduce the scatter significantly, but for the other samples, normalization improved the precision of the extrapolated D_E values. A weighted mean of the plateau segments in Figure 7A was used in age calculation, though the apparent (at 1σ) decline in D_E value with higher preheating is not understood.

Sample EK98-5 (TIBT 98-2) was collected from laminated lacustrine sediments along the Min Jiang, ~50 km south of the Min Jiang basin. Lacustrine sediments are interbedded with tributary alluvial fans along the river, which are correlative with fans of Q_3 age in the headwater reaches (Fig. 4). The resulting apparent age of 14.2 ± 1.7 ka (Table 3) broadly agrees with ^{14}C ages up to ~15 ka for Q_3 terrace gravels in the headwaters of the Min Jiang and lends a measure of confidence to our IRSL results. Silts within the lacustrine deposits appear to have been effectively zeroed by sunlight during transport and residence in the water column.

Two samples were collected from the Q_1 deposits (Fig. 5). Sample EK 98–9 (TIBT 98-4) was collected from fine silts and reworked loess near the base of Q_1 (~15 m above the basal contact with bedrock). The sample yielded an IRSL age of 254 ± 35 ka. A second sample (EK 98-6 / TIBT 98-3) collected from the 1-m-thick loess paleosol atop Q_1 conglomerates near Zhangla

TABLE 2. DOSIMETRY DATA FOR IRSL SAMPLES FROM THE MIN JIANG BASIN

Sample (TIBT)	Water*	K_2O (wt%) (±0.05)	C_t[§] ($ks^{-1}\cdot cm^{-2}$)	C_{th}[§] ($ks^{-1}\cdot cm^{-2}$)	Th (ppm)	U (ppm)	*b* value[#] $pGy\cdot m^2$	Dose rate** (Gy/k.y.)
98-2	0.10 ± 0.05	2.13	0.712 ± 0.010	0.403 ± 0.037	10.84 ± 0.98	2.46 ± 0.30	0.923 ± 0.091	3.82 ± 0.23
		2.18[†]	0.674 ± 0.010	0.285 ± 0.020	7.68 ± 0.70	3.03 ± 0.20		
98-3	0.18 ± 0.03	2.43	0.8540 ± 0.0098	0.495 ± 0.036	13.32 ± 0.97	2.81 ± 0.29	1.0 ± 0.1	4.28 ± 0.16
		2.85	0.836 ± 0.010	0.469 ± 0.033	12.6 ± 1.0	2.87 ± 0.20		
98-4	0.10 ± 0.05	1.05	0.4858 ± 0.0079	0.164 ± 0.022	4.41 ± 0.59	2.51 ± 0.18	1.0 ± 0.1	2.83 ± 0.19
		2.26[†]	0.710 ± 0.048	0.323 ± 0.042	8.7 ± 1.2	3.03 ± 0.20		

*Estimated average historic ratio of weight of water/weight of dry sample, based on measurements of moist collected samples and laboratory saturated samples (3 samples per IRSL sample). Uncertainties here and elsewhere are ±1σ.

[†]From top to bottom, estimated uncertainty in these values is ±0.09 and ±0.25.

[§]Total and thorium count rates from finely powdered samples for thick-source-alpha-particle-counting (TSAC) method (Huntley and Wintle, 1981). $C_u = C_t - C_{th}$. Equations for the use of these count-rate values in the calculation of dose rate are given by Berger (1988). A second row of data corresponds to the average values from sediment surrounding the IRSL sample at a radius of 12–23 cm. These data are used to calculate the γ dose-rate component.

[#]Alpha effectiveness factor (Huntley et al., 1988; Berger, 1988). Values of 1.0 are estimated (from this and other projects).

**Calculated with the conversion factors and equations given by Berger (1988), and includes a cosmic ray component varying from 0.04 to 0.14 with estimated average depth, from the data of Prescott and Hutton (1988). Note that the dose rates are typical of most sediments (2–4 Gy/k.y.).

TABLE 3. IRSL DATA AND AGES FOR LUMINESCENCE SAMPLES

Sample (TIBT)	Preheat*	D_E[†] (Gy)	Time[§] (s)	Age (ka)
98-2	135 °C/2d	61.3 ± 4.1	1–40	
	155 °C/2d	49.3 ± 3.4	1–40	
	Weighted mean D_E =	54.2 ± 5.9		14.2 ± 1.7
98-3	150 °C/2d	710 ± 180	20–60	
	170 °C/2d	640 ± 160	1–35	
	Weighted mean D_E =	670 ± 120		157 ± 28
98-4	140 °C/2d	730 ± 130	1–15	
	160 °C/2d	710 ± 130	1–15	
	Weighted mean D_E =	719 ± 92		254 ± 35

Note: The polymineralic 4–11 μm size fraction was used for all IRSL measurements. IRSL was detected at the 420 ± 20 nm spectral region (bandpass 390–470 nm at 1% cut). All bleaching was for 3 hr with >780 nm solar spectrum passed (based on the bleaching protocol introduced by Huntley and Clague, 1996). Applying the heat treatment after bleaching corrects for any possible thermal-transfer effect (Ollerhead et al., 1994), an apparently negligible effect with these samples.

*The chosen prereadout annealing. For all samples, the weighted mean D_E is used for age calculation (see text).

[†]Weighted mean equivalent dose plus average error over time interval in next column. A weighted-saturating-exponential regression and error model (Berger et al., 1987) was employed for all samples. For some samples, interaliquot scatter was minimized by short-shine normalization (to natural signals) (Ollerhead et al., 1994).

[§]The readout (LED-on) time interval for which D_E is calculated (e.g., Fig. 7).

(Fig. 4) yielded a luminescence age of 157 ± 28 ka. Without independent age determinations, the IRSL results must be taken as a best approximation of the depositional age. However, we note that both of our age determinations fall within known periods of loess deposition in north-central China (Kukla, 1987). Together, these samples indicate that most of the sedimentation in the Min Jiang basin took place in a short time period between ca. 250 ka and 160 ka.

Chen et al. (1994) reported two thermoluminescence (TL) ages of 158 ± 12 ka and 830 ± 69 ka for samples from the Guyian Shan Formation (mapped as Q_1; Fig. 4). The first sample was taken "from the base of the loess" covering the formation and therefore may be correlative with the paleosol between Q_1 and Q_{1-2} (157 ± 28 ka). Their second sample was taken "50 m down in the Guyian Shan Formation." Chen et al. (1994) provided no information about the material in the horizon sampled, except that formation "is composed of thick beds (1–3 m) of conglomerate interbedded with thin (10–30 cm) beds of sandstone." Considering the likelihood of rapid (poor TL-zeroing) deposition in these types of deposits and the general question of the upper limit of TL dating techniques (Berger, 1995; Prescott and Robertson, 1997), we cannot assess the accuracy of the older TL age, except that it is likely an overestimate. Our ages are also significantly younger than ages typically assigned to "Q_1" deposits throughout southwestern China (ca. 1.6–0.6 Ma) (Ministry of Geology and Mineral Resources, People's Republic of China, 1991), which suggests caution in interpreting absolute age from regional correlation of terrestrial Quaternary deposits in western China.

Our results further suggest that periods of deposition were tied to glacial-interglacial cycles. The onset of Q_1 deposition occurred shortly prior to ca. 250 ka and appears to coincide with oxygen isotope stage 8 (Imbrie et al., 1984). Loess deposition between Q_1 and Q_{1-2} (ca. 160 ka) coincides with the stage 6 termination (Imbrie et al., 1984), and this loess may be correlative with the L_2 loess of the Upper Lishi Formation in well-studied sections on the Loess Plateau (Kukla, 1987). Aggradation of Q_2 fluvial terraces is not well dated in the Min Jiang basin, but may date to ca. 22 ka (e.g., ^{14}C from Ningpo sediments), near the time of the last glacial maximum (Imbrie et al., 1984). Aggradation of the Q_3 terrace occurred between ca. 15 ka and ca. 6–7 ka, coincident with isotope stage 2. Thus, fill-terrace development along the headwater reaches of the Min Jiang was apparently coincident with the last glacial period. Incision of the Min Jiang into the Q_3 terrace gravels appears to postdate 6 ka. These results are striking in their correlation to late Pleistocene climatic oscillations (Imbrie et al., 1984) and suggest that late Quaternary terrestrial deposition in the Min Jiang basin was closely coupled to changing sediment and water flux during glacial-interglacial cycles.

QUATERNARY FAULTING IN THE MIN SHAN

Quaternary deposits within the Min Jiang basin are variably deformed (Fig. 4) and place important constraints on the kinematics and rates of Quaternary deformation in the Min Shan. We first consider the recent and active displacement along the Min Jiang fault and then examine several important structures within and east of the range.

Min Jiang Fault

The Min Jiang fault zone consists of several strands of high-angle reverse faults that strike approximately due north and parallel the western

side of the Min Shan for nearly 100 km. The easternmost strand bounds the western margin of the Min Jiang basin and juxtaposes Triassic limestone and flysch with terrace deposits along the Min Jiang river (Chen et al., 1994; Tang et al., 1993; Zhao et al., 1994). Although many of these authors consider the fault to be active, recent GPS results from a station west of the fault zone (station SBP2; Fig. 2) suggest that short-term displacement rates are less than several millimeters per year and within uncertainty of zero (Chen et al., 2000; King et al., 1997). In addition to uncertainty regarding the Holocene slip rates of the fault, previous workers disagreed on the sense of displacement. All have agreed that there is a strong component of shortening across the fault, but the strike-parallel component has been interpreted as both dextral and sinistral (cf. Chen et al., 1994; Zhao et al., 1994). We mapped the easternmost segment of the fault (herein referred to as the Min Jiang fault, sensu stricto) from north of Gonganin (Fig. 4) to the town of Songpan (Fig. 3).

The southern part of the Min Jiang fault follows the eastern side of the Min Jiang valley between the towns of Chuanjiusu and Songpan (Figs. 3 and 4). The fault, although not well exposed, offsets tributary drainages and gullies along the eastern valley wall. Seven of nine tributary gullies along this stretch of the fault appear to be deflected in a manner consistent with a component of left-lateral displacement along this segment of the fault (Fig. 6D). We were unable to map the fault south beyond Songpan, although a series of northwest-striking folds in the Triassic appears to be continuous across the projection of the Min Jiang fault (Fig. 3). Thus, we infer that the displacement on the fault diminishes along strike to the south or is transferred to distributed shortening.

Along the southern part of the Min Jiang basin, a north-striking, west-dipping splay of the Min Jiang fault (herein named the Ningpo fault after a nearby village and monastery) juxtaposes fine-grained sands and gravels in its hanging wall (Q_2 in Fig. 4) with the Q_1 conglomerates to the east. Gravels west of this fault are warped into an asymmetric anticline with a north-trending axial trace (Fig. 4). The Ningpo fault can be followed as a discrete break between the Q_1 and Q_2 deposits for ~1 km to the north, whereupon the trace of the fault transfers into the axial trace of an open syncline (Fig. 4) within the Q_1 gravels. The geometry of the folding within both the Q_1 and Q_2 deposits suggests that the fault has a component of west-side-up, reverse displacement, akin to the Min Jiang fault. It is noteworthy that this is the only part of the basin where a fault coincides with the eastern basin margin.

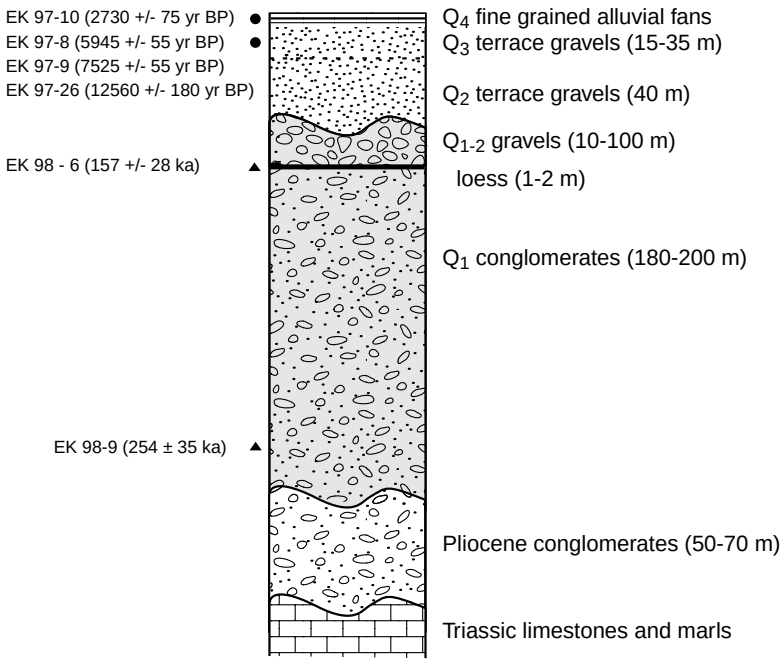

Figure 5. Schematic composite stratigraphic column of Tertiary–Quaternary sediments of the Min Jiang basin. Coarse pattern represents cobble to boulder conglomerates along Min Jiang fault (white) and Q_1 alluvial-fan conglomerates (gray). Loess interlayer is shown as heavy black line. Fluvial-terrace gravels of modern Min Jiang drainage (Q_2 and Q_3; fine-dot pattern) are overlain by Q_4 alluvial fans (ruled pattern). Approximate sample locations are shown along the left side of the column (radiocarbon—circles, IRSL—triangles).

The Ningpo fault is joined by an east-trending fault east of Chuanjiusu (Fig. 4). This fault dips ~60°N and is marked by a 10–20-cm-wide gouge zone within the Q_2 sediments in the valley bottom. The separation on the fault appears to be north side up, and the fault may have a right-lateral component. The fault appears to transfer displacement between the Min Jiang and Ningpo faults, some of which may be accommodated by folding of Q_2 sediments west of the Ningpo fault.

The Min Jiang fault itself is best exposed in a small drainage west of the town of Zhangla, in the southern end of the Min Jiang basin (Fig. 4). Here the fault dips 55°–65°W and places brecciated Triassic limestone above Q_2 terrace gravels. A 1–3-cm-wide zone of clay-rich red gouge marks the fault zone. The Q_2 terrace is inset along this segment of the Min Jiang valley into older $Q_{1–2}$ gravels. These deposits are mixed alluvial gravels and breccias of angular limestone clasts derived from the Triassic in the hanging wall of the Min Jiang fault.

Approximately 4 km north of Zhangla, the $Q_{1–2}$ gravels pinch out, and the fault places limestone directly over the Q_1 conglomerate. The fault itself is not well exposed along this stretch, but its mapped trace suggests that it dips moderately to the west (Fig. 4). From this point north, there is little evidence for recent displacements along the Min Jiang fault. We infer that the trace of the fault parallels the linear range front between Gamet and Kakagou (Fig. 4); however, exposure is poor along the steep forested slopes. On the western side of the ~4000 m ridge between Gamet and Kakagou, an east-dipping splay of the fault juxtaposes the Triassic with Pliocene conglomerates (Chen et al., 1994), indicating that this strand of the fault zone is relatively young. However, we were unable to find any scarps or morphologic evidence that this splay is active at present. The Triassic limestone between the two strands is interpreted as a pop-up block within the Min Jiang fault zone (Fig. 4).

North of Kakagou, a second strand of the Min Jiang fault zone bounds the western edge of the Min Jiang basin (Fig. 4). This fault is well exposed in the drainage west of Gonganin, dips ~45°W, and places Triassic limestones above $Q_{1–2}$ alluvium. The $Q_{1–2}$ gravels are exposed over ~15 km^2 along the western side of the Min Jiang valley headwaters. Gravels within this subbasin generally dip moderately west and are locally folded into an overturned footwall syncline beneath the western fault strand. They appear to be juxtaposed with Q_1

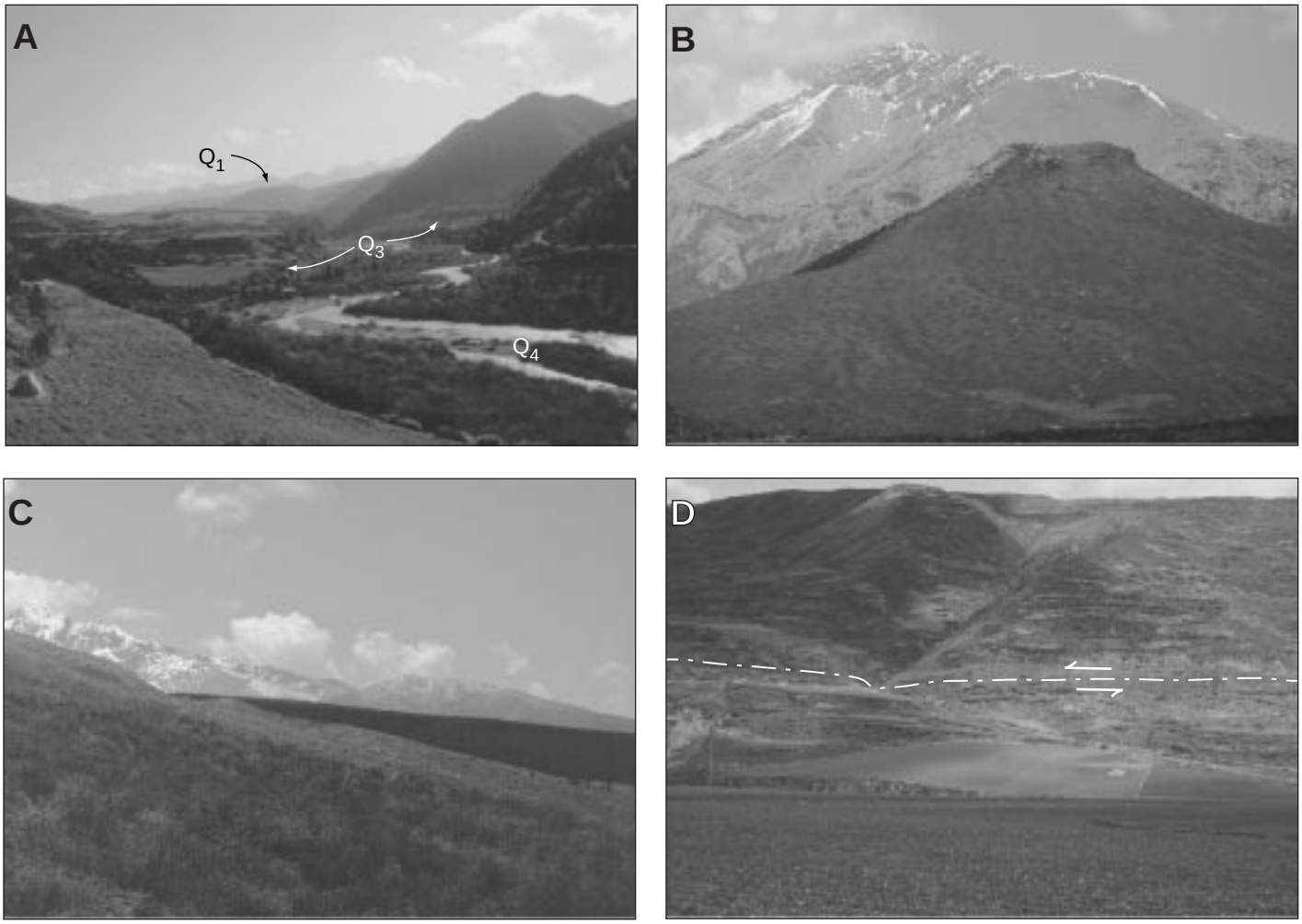

Figure 6. Field photographs of sediments within the Min Jiang basin (A–C) and of the Min Jiang fault (D, E). (A) Looking north at the central Min Jiang basin. West-dipping ridges in the background are composed of Q_1 conglomerates dipping ~14°. Alluvial sediments (late Pleistocene-Holocene) of the Min Jiang river (Q_3, Q_4) fill the valley in the near midground. (B) View looking north-northeast at remnant Q_1 (mesalike hill in midground) in the northern Min Jiang basin. Hill is ~170 m high. Ridge in background is composed of west-dipping Triassic limestones. (C) Tilted bedrock surface beneath basin extends along ridge tops toward crest of range. Photograph is looking south along the eastern edge of the Q_1 conglomerates. Snow-capped peak is Hong Xin Yan Shan (~ 5100 m). (D) Shutter ridge along the southern Min Jiang fault indicative of a component of left-lateral displacement. Trace of fault shown in white. The terraced fields at the base of the ridge are on a young alluvial fan built across the fault trace. View is to the east. (E) View to the southeast of high erosion surface west of the Min Jiang fault (highlighted by arrow). Min Jiang fault runs along base of ridges (dashed white line). The flat, linear ridges in the foreground at left are Q_2 terraces preserved in the headwaters of the Min Jiang.

conglomerates exposed on high hilltops east of the Min Jiang. However, the contact is obscured by modern alluvium. We infer from the mapped geometries that the eastern strand of the Min Jiang fault forms the eastern boundary of this subbasin. The exposure in the steep forested hillslopes north of the drainage divide is poor, and consequently the northern extent of this structure is uncertain. However, the western strand of the Min Jiang fault clearly continues to the north, where it juxtaposes Triassic limestones and Pliocene gravels (Fig. 4). Our interpretation of these geometries is that much of the displacement on the eastern Min Jiang fault transfers to the western strand across the subbasin of Q_{1-2} gravels.

Long-Term Displacement on the Min Jiang Fault

The morphology of the Tibetan Plateau to the west of the Min Jiang fault places loose bounds on the total displacement across the fault. Preserved remnants of a low-relief erosion-surface cap ridge crests west of the Min Jiang fault (Figs. 4 and 6D). This surface is ~200–300 m above the modern valley of the Min Jiang. Although bedrock surfaces are continuously evolving elements in an active landscape, the low relief and partial preservation of the surface suggest that erosion rates on the surface proper are probably low. We interpret the surface as the western continuation of the low-relief surface that floors the Min Jiang basin. This correlation must be considered tentative, but, if correct, implies a net throw on the Min Jiang fault of between ~350 and ~750 m. Thus, the Min Jiang fault does not appear to have a significant amount of displacement across it in the late Cenozoic.

Timing of this displacement is, however, uncertain. The age of the erosion surface in the Min Shan is essentially unknown. Our mapping indicates that it must be older than the Q_1 conglomerates (ca. 250 ka), but its relationship to the Pliocene(?) deposits is unclear. Regionally, much of the surface of the northeastern Tibetan Plateau is morphologically similar: a low-relief surface cut on vertically foliated Triassic flysch. However, the few Tertiary sediments that exist are not well dated. Consequently, all we can determine is that reverse-sense displacement on the Min Jiang fault appears to be late Cenozoic, and the initiation of movement likely predates the deposition of Q_1. If we assume that the Pliocene basins along the fault zone mark the onset of displacement, long-term slip rates must be significantly less than 1 mm/yr. We conclude that shortening across the Min Jiang fault is likely to have been relatively minor during the Quaternary.

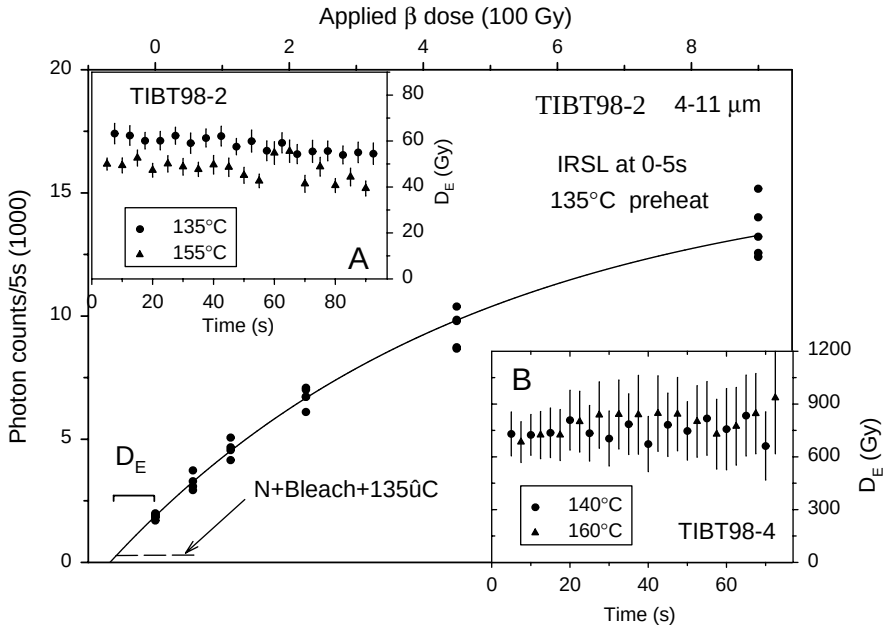

Figure 7. Illustrative luminescence (IRSL) dose-response curve (center) and plots of equivalent-dose (D_E) vs. readout time (inserts A and B). A weighted-saturating-exponential regression model was used for all samples. Error bars on the D_E plots are ±1σ. Equivalent-dose data for 155 °C (inset A) and 160 °C (inset B) are shifted by +2.5 s for clarity of plotting.

Terrace Profiles and Recent Displacements Along the Min Jiang Fault

The modern Min Jiang and associated Q_3 (Holocene) terrace cross the Min Jiang fault in three places within the study area (Fig. 4). In each locality there are no visible breaks or offsets in the terraces. Although this continuity suggests that there has been little displacement on the fault in Holocene time, we surveyed the modern channel and terrace profiles to assess whether low rates of motion on the fault were manifested in changes in the gradient of the channel system and/or terraces (e.g., Pazzaglia et al., 1998). Details of the surveying procedure are given in the Appendix.

The modern channel and Q_3 terrace surface onlap the fault just southwest of the town of Maur Ji (Fig. 4). The terrace gravels are unusually well indurated here, and the channel is fairly narrow. However, there are several cold springs and associated tufa mounds that mark the trace of the fault, and we infer that the competence of the gravels in this locality reflects the local groundwater flux. The terrace surface does not appear to be deformed within the resolution of our survey (~2 m; see Appendix). The terrace surface is nearer to the modern channel along this reach of the Min Jiang (Fig. 8), however, and we interpret this proximity as reflecting the increased stream gradient as the river flows over resistant limestone. Approximately 5 km north, the fault crosses back to the western side of the Min Jiang and is buried beneath a large landslide mass just south of the Gamet monastery (Fig. 4). This slide mass is composed of angular, shattered blocks of Triassic limestone, and onlap relationships between Q_3 terraces on either side of the slide mass indicate that the slide predates the terrace. Both of these relationships suggest that the Min Jiang fault has had little displacement along it during Holocene time.

South of Chuanjiusu, the fault crosses the river for a third time and is also obscured by a small landslide. There is a small strath terrace beveled into the toe of the slide, which appears to be continuous with the Q_3 terrace. Previous workers suggested that the Q_3 terraces were unusually high along this reach of the Min Jiang, a fact they attributed to recent displacement on the adjoining Xue Shan fault (Chen et al., 1994; Tang et al., 1993); our survey fails to confirm this conclusion. The Q_3 terrace is continuous between Chuanjiusu and Songpan (Fig. 8). Several large alluvial fans onlap the terrace surface near the mouths of larger tributary streams. Although there is significant relief (up to 80 m) on the fan surfaces, they do not represent warping of the main terrace tread.

Mapped relationships between the Min Jiang fault and terraces along the Min Jiang indicate that the youngest displacement on the fault is bracketed between deposition of the Q_2 gravels and the Q_3 terrace. There does not appear to have been significant displacement on the fault during the past ~7000 yr. Given the uncertainties of our sur-

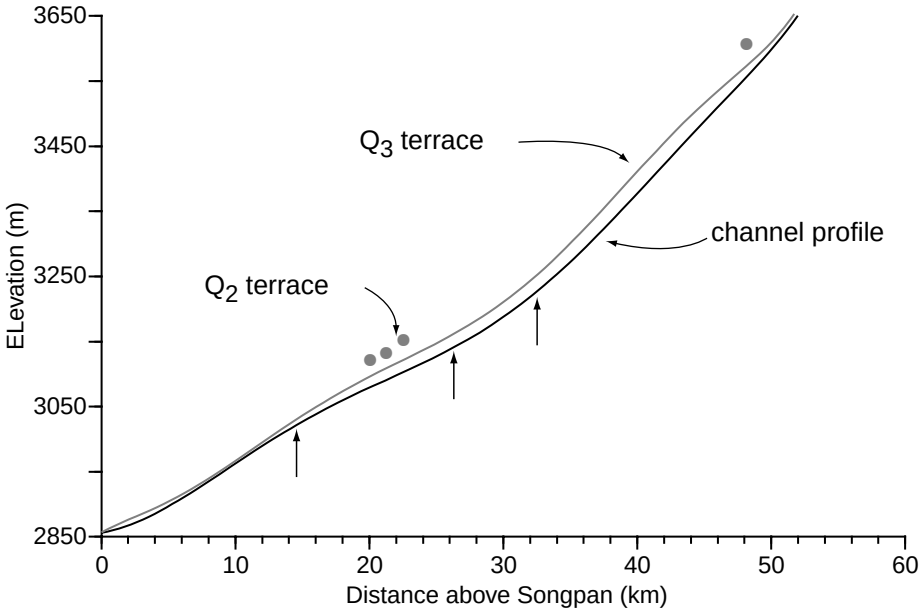

Figure 8. Longitudinal profile of the Min Jiang (black) and Q_3 terrace surface (gray) surveyed between Gonganin and Songpan. Gray dots represent discontinuous Q_2 terrace surfaces. Arrows show the intersection between the trace of the Min Jiang fault and the river channel. Note the smooth transition of the Q_3 terrace across the northern two intersections. Downstream of the final intersection, the channel steepens and the terrace undergoes a transition to a bedrock strath bench ~1–3 m above the river. This change may reflect slight differential rock uplift between the hanging wall and footwall of the Min Jiang fault.

vey (±2 m), there is no appreciable deformation of the Q_3 terrace, requiring Holocene displacement rates to have been less than ~1 mm/yr. This conclusion is consistent with the short-term rates observed in the geodetic data (King et al., 1997). However, the Min Jiang fault cuts Q_2 (late Pleistocene) gravels west of Zhangla (Fig. 4). These relationships are consistent with displacement occurring during moderate to large seismic events with long recurrence intervals (>7000 yr). In addition, the transition from alluvial to strath terraces south of Chuanjiusu coincides with the point where the valley of the Min Jiang is on the hanging-wall block and may reflect bedrock incision in response to slightly increased rates of rock uplift. Although this incision may be an indication of activity on the Min Jiang fault, a quantitative assessment of this hypothesis is beyond the scope of this paper.

Huya Fault

The structural position of the Huya fault along the eastern flank of the Min Shan (Fig. 3) and the historic seismic activity along it (Jones et al., 1984) suggest that this fault may play an important role in active deformation along the Min Shan. However, the mapped extent of the fault (Ministry of Geology and Mineral Resources, People s Republic of China, 1991) along the central ~60 km of the range (Fig. 3) suggests that displacement diminishes along strike or is transferred to distributed deformation. In order to assess these possibilities, we examined the Huya fault in reconnaissance fashion along much of its length. The central segment of the fault crops out along the Fu Jiang, where it dips steeply west (70°–90°) and juxtaposes Paleozoic limestones of the Xue Shan platform with metamorphic rocks mapped as Precambrian (Fig. 3). These geologic relationships (younger over older) are unusual for a reverse fault and suggest that the Huya fault may have a pre-Cenozoic ancestry. Along the valley of Fu Jiang, the fault cores a steep rugged canyon and is spatially associated with numerous rockfalls and landslides, the most recent of which are presumably the result of the 1976 earthquakes (Jones et al., 1984).

The Huya fault terminates to the north against the Xue Shan fault and to the south against the Qingchuan fault (Fig. 3). These relationships at the terminations of the Huya fault have important implications for the transfer of displacement along the eastern range front of the Min Shan. Although it is possible that the Huya fault is a blind structure along the range front north of the Xue Shan fault, the apparent continuity of Paleozoic and Mesozoic units across the range front (Fig. 3) suggests that the total amount of displacement must be relatively small. This geometric relationship at the north end of the Huya fault requires that displacement across it must decrease along strike to the north or be accommodated by distributed deformation between the Xue Shan and Tazang faults (Fig. 3).

A similar relationship exists at the southern end of the Huya fault where Triassic rocks west of the fault are folded around its southern termination and are continuous with Triassic rocks along the Qingchuan fault (Fig. 3). Although the Qingchuan fault makes a remarkably linear trace on satellite images (Fig. 2), geodetic results (Chen et al., 2000; King et al., 1997) suggest that active displacement on the Qingchuan fault is restricted to a few millimeters per year of right-lateral displacement. Our reconnaissance observations of undeformed Pleistocene terraces along the Fu Jiang (E. Kirby, unpublished data) suggest that shortening is negligible. Although the Qingchuan fault may represent a component of right-lateral shear northeast of the topographic margin of the plateau, it does not appear to absorb displacement along the Huya fault. Thus, displacement along the southern Huya fault is likely transferred to small, discontinuous structures of similar orientation in the southern Min Shan (Fig. 3).

Xue Shan Fault

The Xue Shan fault is an west-trending zone of faults that terminate against the Min Jiang fault north of the town of Songpan (Figs. 3 and 4). The fault extends beyond the modern topographic margin of the plateau into the foreland, where it carries Paleozoic rocks in both its hanging wall and footwall (Fig. 3). These geometries suggest, but do not require, relatively minor displacement across the fault. At its eastern end, the Xue Shan fault is intruded by a Mesozoic pluton, indicating that much of the displacement predates Mesozoic magmatism (Ministry of Geology and Mineral Resources, People's Republic of China, 1991). We were unable to verify proposed recent activity along the Xue Shan fault (Tang et al., 1993) near the crest of the range. Such displacement, if present, appears to be limited, and we interpret the Xue Shan fault as a Mesozoic structure that has played a minor, if any, role in Cenozoic deformation within the Min Shan.

RATES AND PATTERNS OF SURFACE DEFORMATION IN THE MIN SHAN

In spite of the apparently minor displacement along the Min Jiang and other faults west of the Min Shan, there is abundant evidence for tilting of Pleistocene–Holocene markers within the range. In this section we describe tilting recorded

in two places within the western Min Shan: (1) in young lacustrine sediments along the Min Jiang and (2) within the Min Jiang basin. In both localities, tilting is present over 10–20 km wavelengths and does not appear to be directly associated with exposed faults.

Recent Tilting in the Southern Min Shan

Recent tilting is recorded in the southwestern Min Shan in lacustrine sediments north of the Diexi landslide. The Diexi landslide is a large (~1 km^3) slide mass that dammed the Min Jiang drainage near the village of Jiaocheng (Fig. 3). This site is located near the epicenter of a moderate-sized earthquake in 1933 that initiated a rockslide obliterating the village of Diexi (Chen et al., 1994). The prehistoric slide, however, is preserved on both sides of the valley and appears to have dammed the entire Min Jiang. The surface of the slide is ~200 m above the current river level and preserves characteristic hummocky topography, draped with ~1 m of loess. Some large boulders are visible atop the slide mass.

Deposits of lacustrine sediments as thick as 30 m occur upstream from the landslide mass for nearly 25 km along the Min Jiang. These deposits are typically preserved beneath abandoned alluvial fans debauched from side-tributary drainages, although drapes of sediment can be seen high on a few hillslopes. We correlate these fans with the Q_3 tributary alluvial fans in the Min Jiang basin (Fig. 4). The lacustrine sediments are extremely fine-grained silts and muds, have a characteristic yellow color, and are generally laminated on a millimeter scale. The original thickness of many of the deposits does not appear to be preserved, and often overlying fan material has cut deep channels into the silts.

We surveyed the relative elevations of the preserved lake sediments along the valley for 21 km north of the slide (survey techniques are presented in the Appendix). The northernmost remnants of demonstrably lacustrine sediment range from 20 to 40 m above the elevation of the slide surface at Jiaocheng (Fig. 9). We referenced all elevations to the lowest point on the upstream side of the dam where we could discern the original surface of the slide. The edge of the remnant slide on the opposite valley wall is present at almost the same elevation (1–2 m higher), and we are confident that, although the original spillway could have been lower than our estimated position, it could not have been higher. Furthermore, we consistently surveyed the highest-preserved sediments; any subsequent erosion would serve to reduce this estimate. Although our inference of tilting relies on a few exposures of sediment at elevations higher than the slide, these elevations are minimum estimates of the original elevations, and our estimate of the degree of tilting is likewise a minimum.

We obtained a sample of the lacustrine sediments for IRSL dating (see Appendix for analytical procedures and Tables 2 and 3 for results). Sample EK 98-5 (TIBT 98-2) was collected from a 10 m face of wavy, laminated lacustrine muds ~19 km above the landslide. The sample gives an age of 14.2 ± 1.7 ka and is within error of our estimate for the age of Q_3 deposits upstream (6–13 ka). Given 20–40 m of tilting over a 21 km base line, this age implies tilting rates of 6.6×10^{-8} to 1.4×10^{-7} rad/yr. At the northern end of the former lake, this range translates to differential rock uplift rates of 1.4–2.8 mm/yr. These rates are fairly rapid given the apparent absence of geodetically detectable shortening across the range. The linear geometry of the deposit, unfortunately, allows us to resolve only the north-south component of the tilting; any east-west component remains unknown.

Pleistocene Tilting of Q_1 and Relief Development in the Min Shan

East-west tilting is recorded in the west-dipping Pleistocene Q_1 conglomerates east of the Min Jiang fault. Q_1 deposits are preserved over nearly 175 km^2 of the Min Jiang basin (Fig. 4). Over most of this region, the conglomerates strike 010° to 040° and dip ~14°NW (Fig. 4, inset). The only exception occurs at the southern end of the basin, where the gravels are gently folded. Throughout the rest of the basin, they are preserved on long west-sloping ridges between deeply incised tributary drainages (Fig. 6A). The present-day eastern extent of the basin is defined by the onlap of these conglomerates onto an ~15°–18°W-dipping bedrock surface of very low relief (Fig. 6C). This surface extends from beneath the conglomerates and continues to elevations exceeding 4200 m along the west flank of the Min Shan (Fig. 4).

Determining the magnitude of the tilting recorded in the Q_1 conglomerates depends largely on an estimate of the initial slope. Depositional slopes of terrestrial deposits can vary widely, depending on the nature of the transport process, sediment size, and fine sediment content (e.g., Blair and McPherson, 1994). However, three lines of evidence lead us to conclude that the depositional slope of the Q_1 conglomerates in the Min Jiang basin was fairly shallow. First, the deposits are alluvial in character. All exposures of the Q_1 conglomerates are clast-supported gravels interbedded with fine sands and silts. The finer-grained layers dip concordantly with the coarser gravels. We found no exposures within the Q_1 conglomerates of debris-flow deposits or of glacial till. Compilations of the slopes of modern alluvial fans in a wide range of environments indicate that depositional slopes on fans dominated by alluvial deposits rarely exceed 3°–4° (Blair and McPherson, 1994). Second, measurements of the surface slope on undeformed Q_2 terraces preserved in the tributary valleys east of Gonganin (Fig. 4) range from 1° to 3°. Although these may not be a direct analogue for the earlier deposits, the Q_2 terrace gravels are of similar grain size and composition and were likely deposited on a similar depositional slope. Third, we were able to estimate the paleoflow depth from preserved channel geometries, and we measured the median grain size at one locality within the

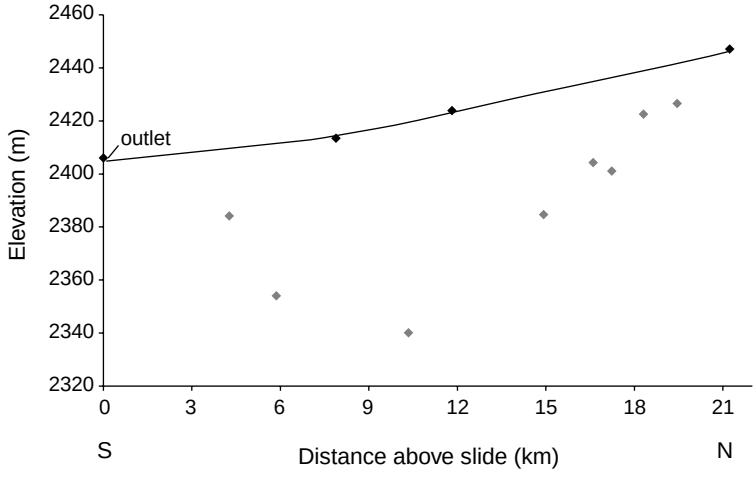

Figure 9. Survey results of lacustrine sediments associated with the Diexi landslide in the southern Min Shan (see Fig. 3 for location). Gray symbols represent localities where the deposits had been eroded. Black symbols represent the upper extent of deposits with no definitive evidence for subsequent erosion.

Q_1 conglomerates. This approach yielded a paleoslope estimate of <1° (Paola and Mohrig, 1996). Although a single measurement may not be a reliable indicator of the regional dip, taken with the other lines of evidence, it suggests that the Q_1 conglomerates were deposited with a shallow initial slope. In the discussion that follows, we make a conservative estimate that the initial slope was ~4°. This estimate is at the high end of the range of likely depositional slopes and thus represents a maximum value.

Given the present mean dip of the Q_1 conglomerates (~14°NW; Fig. 4), the analysis above indicates that the Q_1 has been tilted by at least 10°. The spatial extent over which it occurred indicates that down-to-the-northwest tilting represents a significant component of Quaternary deformation along western flank of the Min Shan. Our mapping demonstrates that there are no faults exposed between the eastern edge of the basin and the crest of the Min Shan. Young faults cut the Q_1 conglomerates only in the southernmost end of the basin (Ningpo fault; Fig. 4). North and east of this region, the conglomerates dip uniformly to the west-northwest. Preserved remnants of the subbasin erosion surface extend nearly to the crest of the Min Shan (Fig. 6C) and suggest that the western part of the range behaved as a relatively coherent block during late Quaternary deformation.

Simple geometric considerations suggest that tilting of the Q_1 conglomerates can account for most of the modern relief between the Min Shan and the plateau to the west. Q_1 gravels are preserved as far as 6 km east of the Min Jiang fault; the erosion surface upon which they were deposited is preserved as far as 9 km east of the fault. Tilting of 10° over these horizontal base lines (3–6 km for the Q_1 and 7–9 km for the subbasin surface) leads to differential rock uplift of 500–1000 m at the eastern edge of the Q_1 gravels and 1200–1500 m at the eastern edge of the subbasin surface. Projecting this tilting to the crest of the Min Shan (some 12–15 km east of the Min Jiang fault) would result in 2000–2500 m of differential rock uplift. Modern relief between the range crest and the Min Jiang valley ranges from 1600 to 2200 m, and it is clear that most, if not all, of it could have developed as a result of Pleistocene tilting. Paleoflow indicators and clast composition suggest that Q_1 deposits were derived from the Min Shan; clearly, there must have been some initial topographic gradient east of the basin. However, the lack of observed structures between the basin and the crest of the range makes a compelling argument that the much of the modern topography developed during Pleistocene tilting along the western flank of the range.

Inferred rates of tilting within the Min Shan are remarkably rapid. Tilting of 10° in 250 k.y. requires rates on the order of 7×10^{-7} rad/yr. Differential rock uplift rates depend upon the base line chosen, but for the three positions we have already discussed the eastern extent of Q_1, the eastern extent of the subbasin surface, and the crest of the range—rates range from 2.0 to 4.1 mm/yr, 4.8–6.2 mm/yr, and 8.3–10.3 mm/yr, respectively. We stress that these values only reflect differential rock uplift. Inferred mean incision rates of tributary streams through the Q_1 and the underlying bedrock approach ~1.5 mm/yr (e.g., ~200 m in ~160 k.y.). The lack of information regarding the lowering rate of hillslopes and ridge crests in the Q_1 deposits and the lack of denudation rates east of the preserved basin margin prevent us from obtaining a quantitative estimate of surface uplift in the Min Shan (England and Molnar, 1990a). However, the preservation of the bedrock surface that floors the basin at elevations approaching the crest of the range leads us to infer that differential surface uplift was very likely positive along the west flank of the Min Shan during the late Pleistocene.

FLEXURAL ISOSTATIC CONTRIBUTION TO TILTING IN THE MIN JIANG BASIN

Some component of the down-to-the-northwest tilting observed in the Min Jiang basin could be attributed to a flexural isostatic response to denudation along the eastern flank of the range. Such a mechanism has been invoked for high mountain ranges flanking both the Tibetan Plateau and Andean Altiplano (Masek et al., 1994b; Molnar and England, 1990; Montgomery, 1994), as well as for high-standing continental escarpments (Kooi and Beaumont, 1994; Tucker and Slingerland, 1994). In order to assess the necessary conditions under which an isostatic response to erosional unloading could significantly influence the deformation observed in the Min Shan, we utilize a simple flexural model. We take two complementary approaches. We first consider the modern topographic relief as the residue from the removal of a distributed load from the lithosphere so that we can model the flexural response to erosional dissection of a plateau margin. Second, we model the effects of uniform erosional unloading of the eastern flank of the range and ask how much mass removal is required to produce the observed tilting (deflections) in the Min Jiang basin.

In our first model, the load removed from the lithosphere is calculated from the topographic relief in the landscape. We utilize a digital elevation model of the topography in eastern Tibet (90 m nominal resolution, data set described in Fielding et al., 1994) and extract the topographic relief along a 75-km-wide swath oriented perpendicular to the topographic margin of the plateau (see Fig. 2 for location). The swath width was chosen to enclose the entire upper drainage basin of the Fu Jiang, the major river draining the eastern Min Shan, and so provides a relatively complete picture of the relief structure of the landscape east of the Min Shan. We binned elevations across the swath and calculated local relief as the difference between the maximum elevation and all other elevations within a bin. This is functionally equivalent to fitting a surface to peak elevations and extracting the difference between that surface and the landscape (Montgomery, 1994). However, by measuring relief along the entire channel system, we obtain a volumetric estimate of local valley-bottom to ridge-top relief. Relief is averaged in each bin to obtain an estimate of the mean relief along the chosen swath. This quantity is imposed as a distributed surficial load removed from the lithosphere.

We model the lithospheric response to removal of this topographic load as that of a thin, uniformly rigid elastic plate overlying a viscous substrate (Turcotte and Schubert, 1982; equation 3.125). In the discussion that follows we use the term "flexural rigidity" interchangeably with the term "effective elastic thickness," T_e, where we assume a Young's modulus of 7×10^{10} Pa and Poisson's ratio of 0.25 (Turcotte and Schubert, 1982). The density contrast between the crust and mantle in our model is 600 kg/m^3 (ρ_{crust} = 2700 kg/m^3, ρ_{mantle} = 3300 kg/m^3). The effective elastic thickness and the lateral boundary conditions control the flexural response to the imposed load. End loads in our model are assumed to be zero. We place the load within a model domain that is long (>500 km) relative to the load and force the ends of the model domain to have zero deflection. The modeled deflection is then calculated over the original length of the swath. In this way, we avoid edge effects at the ends of our sampled topography.

The topography of the Min Shan region (Fig. 10) is characterized by a gradual increase in elevation from the Tibetan Plateau in the west to the Min Jiang fault and an abrupt rise in elevation between the Min Jiang fault and the crest of the range. Elevations then fall rapidly toward the foreland. Mean relief across this landscape varies from 200 to 500 m west of the Min Jiang fault, to nearly 2000 m along the eastern flank of the range. In order to facilitate interpretation of the potential isostatic response attributable to this relief, we impose the flexural response on an initially horizontal reference surface (Fig. 10) at the elevation of the Tibetan Plateau at the western end of our swath (~3500 m). We caution that we are not assuming an initial condition of the plateau prior to erosion. The horizontal line simply serves as a marker horizon on which to examine the effects of varying parameters. The imposed load is always the mean relief measured along the swath.

The lack of an independent estimate of the rigidity of the lithosphere in eastern Tibet forces us to model a range of possible values. Results are shown in Figure 10C and are strongly dependent on the modeled rigidity of the lithosphere. For elastic thickness ranging from 30 to 40 km, the potential isostatic response is distributed over a wide region of the eastern plateau. Although these models match the broad rise in topography between the Tibetan Plateau and the Min Jiang fault fairly well, they fail to reproduce the high topography of the Min Shan. Only for elastic thicknesses approaching 4–5 km do the model results produce a deflection of similar wavelength as the Min Shan. This result implies that in order for the deformation observed along the west flank of the Min Shan to be an isostatic response to erosional unloading, the crust of the eastern plateau would have to have extremely low rigidity (~4 to 8 × 10^{20} N·m; T_e = 4–5 km).

An additional constraint can be inferred from the amplitude of the modeled deflections. Even if the lithosphere of the Min Shan region is extremely weak ($T_e \approx 5$ km), the predicted amplitude of the deflection between the location of the Min Jiang fault and the crest of the range is on the order of 500 m (Fig. 10C). This result implies that even if all the present-day relief developed in the last 250 k.y., the isostatic response would not reproduce the observed tilting along the western flank of the Min Shan. We can, however, ask how much additional denudation would be required to generate a deflection of the observed amplitude (inferred to be 2000–2500 m at the crest of the range). Here we assume that all denudation is concentrated along the eastern flank of the Min Shan. Although this is not true in detail, it should allow us to approximate, to a first order, the amount of mass removal necessary to produce a deflection similar to the observed topography of the Min Shan.

The deflection of a point at the uneroded edge of a plateau is a strong function of load width up to the flexural wavelength (for T_e = 5 km, this wavelength is ~45 km; Fig. 11). Removal of a distributed load (of uniform thickness) from a region greater than or equal in width to this distance produces a deflection at the margin with a magnitude equal to ~0.48 of the removed thickness. Consequently, in order to produce a deflection with amplitude of 2–2.5 km, we would have to remove at least 4–5 km of material east of the crest of the range. It is important to note that this simple model also demonstrates that if denudation is focused in a narrow zone (i.e., less than the flexural wavelength) along the range front, the isostatic response is greatly reduced.

Our model results indicate that in order for the observed deformation and topography along the western flank of the Min Shan to be produced as an isostatic response to erosion, two conditions

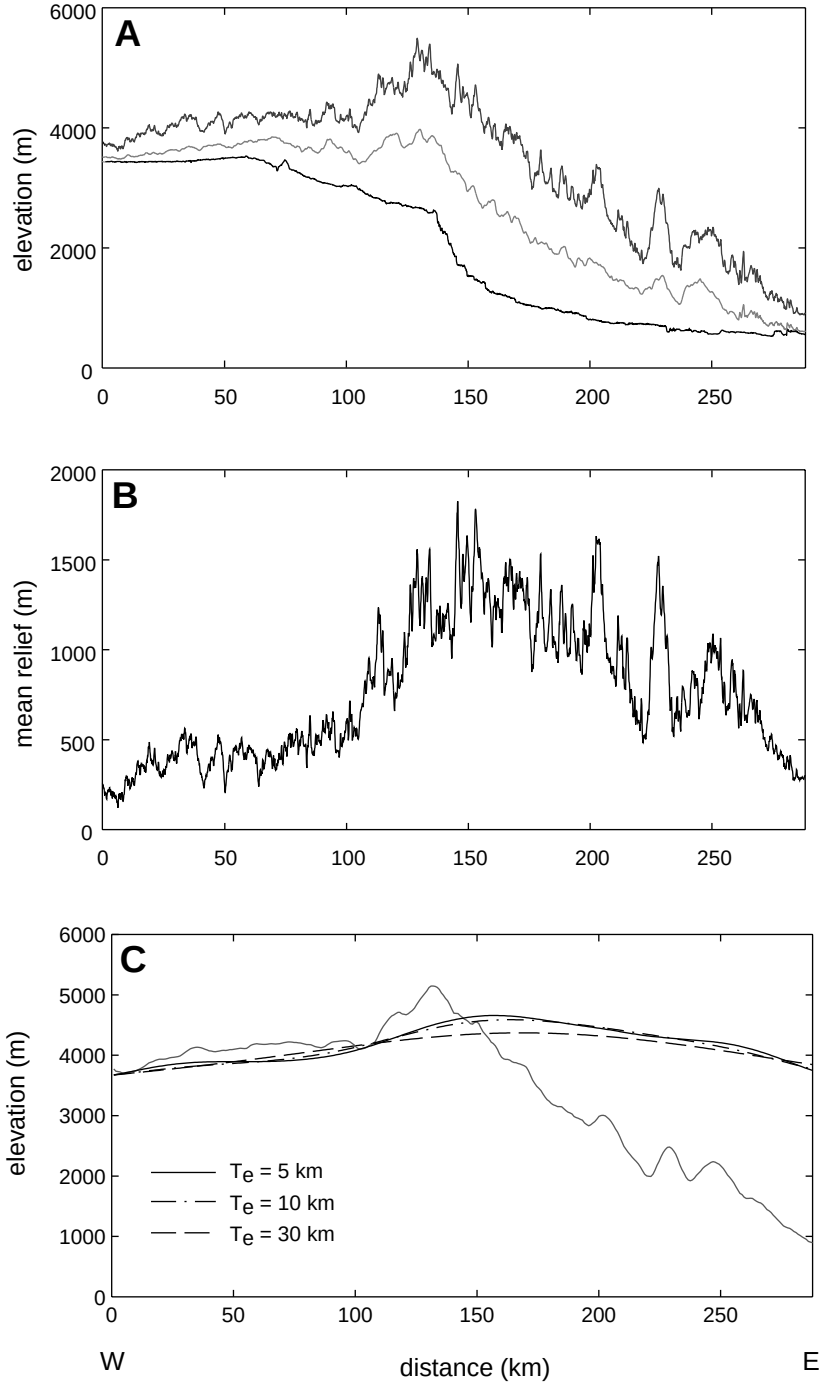

Figure 10. (A) Topographic swath profile across the Min Shan margin. Maximum, minimum (dark lines), and mean elevations (gray) are extracted from ~90 m bins (1 pixel), selected perpendicular to the swath. (B) Mean relief as a function of distance across the Min Shan. This function is used as a distributed line load removed from the lithosphere in our flexural model. (C) Modeled deflections for various T_e values for a reference surface calculated from removal of load in B. Reference surface is originally a horizontal surface at 3500 m. Gray line shows envelope of maximum topography for reference. Details of the calculation are discussed in the text.

must hold: (1) the crust must be extremely weak ($T_e \leq 5$ km), and (2) there must have been 4–5 km of denudation east of the range crest. Unfortunately, little is known about the strength of the lithosphere in this region of the plateau. Estimates of the elastic thickness of the lithosphere in southern Tibet range from 5 to 15 km (Masek et al., 1994a). However, these measurements are in a region of active extension and high heat flow. There is little geologic evidence for such high heat flow in the Min Shan region, and we find it unlikely that the lithosphere has such low rigidity.

Removal of 4–5 km of material in ~250 k.y. from the eastern range front would require denudation rates on the order of 15–20 mm/yr. Existing thermochronologic data from the region are sparse, but bear importantly on the long-term denudation rates along the range. Fission-track measurements in apatite taken from a few localities within the Min Shan (Arne et al., 1997) yield ages between 30 and 120 Ma. Kirby et al. (1999) obtained a cooling trajectory from a small Mesozoic granite at the eastern foot of the range (west of the Huya fault; Fig. 3). Potassium feldspars ($^{40}Ar/^{39}Ar$) and apatite (U-Th-He) from this sample record rapid cooling from temperatures of ~200 °C beginning at ca. 6 Ma. These authors argued that mean denudation rates over this period were probably between 1 and 2 mm/yr. If these denudation rates are representative of the late Quaternary (past ~250 k.y.), they suggest that erosion along the eastern range front was likely limited to 250–500 m. This is an order of magnitude smaller than rates required to produce the observed tilting along the western flank of the Min Shan and suggests that the isostatic component is probably limited to 100–200 m (assuming T_e = 5 km). Thus, the tilting in the Min Jiang basin (and the consequent topography) appears to be primarily a tectonic signature.

DISCUSSION: DYNAMICS OF MOUNTAIN BUILDING IN THE MIN SHAN

The most striking observation regarding the active faulting along the Min Shan is that the active faults bear little relationship to the topographic range front. Although the Huya fault is near the eastern foot of the range, it is discontinuous along strike. North and south of the Huya fault, the topographic margin does not coincide with recognized active faulting. Indeed, in the northern Min Shan (north of the Xue Shan fault), Proterozoic–Triassic rocks form a continuous section that extends from the crest of the range to the foreland (Fig. 3). A similarly intact section occurs south of the Huya fault (Fig. 3). These relationships preclude large-magnitude Cenozoic shortening across the range and are surprising given the profound variation in elevation (and presumably crustal thickness) from the plateau to the foreland. The lack of correlation between active faults and the topographic margin of the plateau is reminiscent of the relationships in the Longmen Shan region to the south (Burchfiel et al., 1995), which have been interpreted as a consequence of shortening focused in a weak middle and lower crust (Royden et al., 1997). The geology of the eastern Min Shan thus argues against a conventional mode of shortening at the plateau margin whereby crustal thickening is absorbed at the surface by large-magnitude thrust faults and is consistent with the hypothesis of Royden et al. (1997).

Late Quaternary deformation within the western Min Shan is similarly enigmatic. The Min Jiang fault, although active in the late Pleistocene, does not appear to have significant Holocene displacement along it. In addition, the sense of displacement across the Min Jiang fault (plateau side up) cannot account for the high topography of the Min Shan relative to the plateau. The slow shortening rates inferred for the Min Jiang fault are consistent with regional horizontal velocities determined by space geodesy. However, the evidence for rapid tilting within the range since late Pleistocene time indicates that significant vertical deformation is localized beneath the Min Shan itself. The absence of faults between the eastern margin of the Min Jiang basin and the crest of the range and the continuity of the subbasin erosion surface suggest that, if discrete structures exist within the Min Shan, they must end at depth beneath the range. Likewise, if the Huya fault extends north along the Min Shan, either as a blind structure or as a series of distributed faults, it could account for tilting along the west flank of the Min Shan. However, projection of 10° of tilt across a base line of 50 km (approximately the distance to the inferred trace of the Huya fault) implies that vertical displacement rates (over the past 250 k.y.) on the fault exceed 35 mm/yr. On a fault dipping 60°W, this projection implies horizontal shortening rates across the fault of nearly 20 mm/yr. These rates are at odds with both the record of historic seismicity (Editorial Board, State Seismological Bureau, 1989) and recent GPS measurements (Chen et al., 2000). Clearly, the Huya fault cannot be directly responsible for the observed tilting in the Min Jiang basin. We infer that late Quaternary tilting along the western flank of the Min Shan reflects deformation localized beneath the range itself, the nature of which remains somewhat enigmatic.

The discrepancy between geodetically observed rates of horizontal shortening (Chen et al., 2000; King et al., 1997) and the tilting rates we infer from our mapping and chronology is a second remarkable result of our work. Insofar as the geodetic measurements are representative of the time-averaged velocity field, they appear to restrict the rates of differential

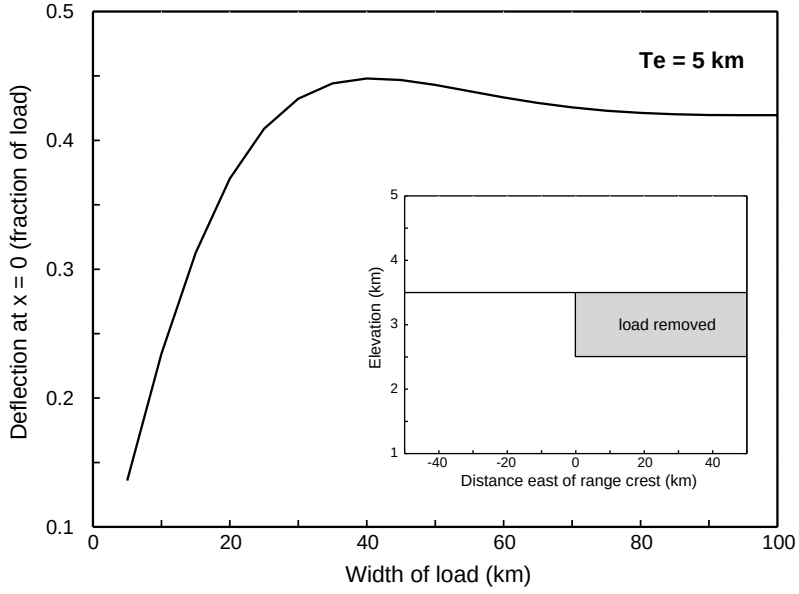

Figure 11. Deflection of an elastic plate as a function of the width of a distributed surface load. Inset shows a schematic representation of load geometry. Load is of constant thickness and variable width. Deflection is calculated at the inner edge of the load ($x = 0$) and roughly corresponds to the divide of a dissected plateau margin. Note that the greatest relief in the Min Shan occurs along the steep eastern range front, over a width of 50–100 km (see Fig. 10); thus (for $T_e \approx 5$ km), we expect deflections at the range crest to be between 0.4 and 0.45 of the load removed.

rock uplift that can be attributed to horizontal shortening to less than 2–3 mm/yr. Although the recurrence interval of seismic events beneath the Min Shan is not well known, the historic record of seismicity contains only four events of magnitude >6 (three of these occurred as part of a single sequence in 1976; Editorial Board, State Seismological Bureau, 1989; Fig. 2). As the record of earthquakes in this region of China extends back over 1500 yr, it seems likely that mean rates of horizontal shortening associated with seismic release are slow.

Although optical dating is still an immature discipline, there is a growing body of empirical evidence (Aitken, 1998; Berger, 1995) that suggests that the technique can resolve depositional ages within 20%–30% over the past 300–400 k.y. The correspondence between our IRSL age for the lacustrine sediments in the southwestern part of the range and ^{14}C ages on correlative terraces lends a measure of confidence to the technique. In addition, our age on the Q_{1-2} loess (ca. 160 ka) corresponds with a time period of documented loess deposition on the Loess Plateau (Kukla, 1987) and suggests that the technique is probably resolving depositional ages. Even if our age estimates are inaccurate by a factor of two, the inferred rates of tilting exceed those attributable to regional horizontal shortening. Although the resolution of this problem awaits further refinement of the Quaternary chronology and/or the establishment of a detailed geodetic survey across the range, we conclude that rapid tilting within the Min Shan is a significant component of the late Quaternary deformation field along this margin of the Tibetan Plateau.

Rapid Holocene tilting observed in lacustrine sediments in the southern Min Shan supports this inference and further highlights the discrepancy between vertical deformation rates inferred from the geology and the lack of significant shortening across the Min Shan. The age of the deposit (ca. 14 ka) indicates that tilting likely took place throughout the Holocene and may be active today. The lacustrine sediments are within 10 km of one GPS station (MJZ1; Fig. 2), which resolves no significant eastward motion relative to the foreland. As in the Min Jiang basin, we find it likely that distributed tilting is an important component of the recent deformation field in the southwestern Min Shan. As vertical velocities are difficult to measure by geodetic means, our work highlights the utility of geologic markers in reconstructing differential rock uplift across regionally significant length scales. In both localities along the Min Shan where geologic markers are present, we find evidence for substantial tilting. We can only speculate as to its importance elsewhere in this region of the plateau.

We have argued above that the observed late Quaternary tilting within the Min Shan cannot be directly attributed to either horizontal shortening or to an isostatic response to denudation at the plateau margin. Although both of these mechanisms undoubtedly contribute to the observed tilting in the Min Jiang basin, even in concert they do not appear to account for the rapid rates we infer from the geometry and age of the Q_1 deposits. Our results thus suggest the presence of an additional driving mechanism. The lack of evidence for large-magnitude Cenozoic shortening along the eastern range front of the Min Shan leads us to consider the possibility that much of the deformation may be driven by flow of a weak lower crust. If the hypothesis of Royden et al. (1997) is correct, lower-crustal material driven from beneath the central plateau may impinge on cold, unthickened crust at the plateau and localize crustal thickening. This scenario is especially true of regions of significant anisotropy (for example, the Sichuan Basin). The presence of pre-Cenozoic structures related to the Xue Shan platform (Min Jiang and Huya faults) may help localize crustal thickening and, to some degree, set the width of the mountain range. We suggest that the observed deformation (both faulting and distributed tilting) in the Min Shan may be a coupled upper-crustal response to thickening localized in the lower crust.

The nature of the coupling between lower-crustal flow and upper-crustal deformation remains somewhat enigmatic, as does the manner in which tilting along the western flank of the Min Shan is accommodated along the eastern range front. Tilting in the Min Jiang basin could represent the western limb of a range-scale antiform with a wavelength of between 50 and 100 km. Alternatively, west-side-up displacement on the Huya fault could be distributed on small discrete structures along the eastern range front between the Xue Shan and Tazang faults. In either case, the lack of significant horizontal shortening across the range appears to require that Quaternary deformation along this segment of the eastern margin of the Tibetan Plateau is driven from below.

ACKNOWLEDGMENTS

This work was supported by the Continental Dynamics program at the National Science Foundation (EAR-961460) and by NASA (NAG 5-6062). We thank B. King, L. Royden, C. Rubin, K. Karlstrom, and M. Clark for helpful discussions on various aspects of this work. B. King kindly helped prepare Figure 2, and L. Royden provided the algorithm for a band matrix inverse solution to the flexural equation. An informal review by C. Rubin and formal reviews by R. Arrowsmith, M. Roy, and F. Pazzaglia led to improvements in the manuscript. Finally, we thank the staff and drivers at the Chengdu Institute of Geology and Mineral Resources for making our work in China possible.

APPENDIX

Survey Techniques

We surveyed the relative elevations of channel profiles, stream terraces, and lacustrine sediments by using a hand-held altimeter (±1 m), clinometer (±0.5°), and laser range finder (±1 m). Uncertainties are quoted from manufacturer specifications. Survey locations were logged by using a hand-held GPS receiver. As the along-channel distance varies with the curvature of the channel, we approximated along-channel distance by using the vehicle odometer (±0.1 km) for the terrace and channel survey. We corrected for daily barometric changes by tracking barometric pressure with a data logger at a fixed location near the center of our survey base line and corrected for these changes over the time of the survey. We estimate that individual measurements are accurate to ~3 m, but that relative differences in elevation (i.e., terrace height above channel) are probably accurate to 1.5–2 m.

Sampling and Analytical Techniques—IRSL Dating

IRSL samples (Table 2 and Figure 5) were collected following the general guidelines found in Aitken (1998). The outer, desiccated face of each outcrop was removed (generally 10–20 cm) taking care to shield the outcrop from direct sunlight. Samples were collected in light-tight Gill Style sample tins and sealed with black tape to preserve moisture content and minimize sample disturbance. In most cases, it was possible to push the tins directly into the sediment, although in one case (TIBT 98–4), a block was carved from the outcrop with a knife. In all cases, the outer 2–3 mm of the block was removed under low-energy light conditions in the laboratory. At each outcrop, three small samples were collected for dosimetry measurements (Table 2). These were spaced over a 50–60 cm distance that bracketed the sample (the effective range of gamma radiation in typical sediment is ~30 cm). For the luminescence measurements, the polymineralic, noncarbonate, detrital, 4–11 μm-diameter size fraction was prepared. Laboratory preparation procedures are outlined elsewhere (Berger, 1990; Wintle and Huntley, 1980).

A luminescence age $t = D_E/D_R$, where D_E is the so-called "equivalent dose," or paleodose (units of Gy [gray], 1 Gy = 100 rads), and D_R is the effective dose rate (Gy/k.y.). D_E is a measure of the postdepositional absorbed ambient ionizing radiation and is derived from luminescence measurements. D_R is derived from independent measurements of U, Th, K, and water concentration. For U and Th measurements, the technique of thick-source alpha-particle counting (TSAC) (Huntley and Wintle, 1981) was applied to dried powders. K was determined by commercial atomic absorption spectrophotometry. Radioactive secular equilibrium is assumed; this assumption is apparently valid for many, although not all, alluvial and fluvial sediments (Olley et al., 1996). Of the available analytical techniques, TSAC can apparently provide a clue to the occurrence of such disequilibrium and, compared to neutron-activation techniques, can provide a more accurate dose-rate measurement for fluvial samples older than ~10 k.y. (Olley et al., 1996).

For IRSL measurements, the deep-blue luminescence near the known 410 nm emission from most K-rich feldspars was chosen for detection (Aitken, 1998). To convert the sample's fossil light to an absorbed-energy equivalent, calibrated laboratory beta (^{90}Sr–^{90}Y) and alpha (^{241}Am) sources were used. The signature was recorded with an automated, high-capacity Daybreak Nuclear Model 1150 reader using an EMI 9635Q photomultiplier tube. Dose-response curves and other data were processed with software produced by one of the authors (Berger; see Berger et al., 1987).

REFERENCES CITED

Aitken, M. J., 1998, An introduction to optical dating: New York, Oxford University Press, 267 p.

Argand, E., 1924, La tectonique de l'Asia: Proceedings, 13th International Geological Congress, Brussels, p. 171–372.

Arne, D., Worley, B., Wilson, C., Chen, S., Foster, D., Luo, Z., Liu, S., and Dirks, P., 1997, Differential exhumation in response to episodic thrusting along the eastern margin of the Tibetan Plateau: Tectonophysics, v. 280, p. 239–256.

Avouac, J. P., and Tapponnier, P., 1993, Kinematic model of active deformation in central Asia: Geophysical Research Letters, v. 20, p. 895–898.

Berger, G. W., 1988, Dating Quaternary events by luminescence, *in* Easterbrook, D. J., ed., Dating Quaternary sediments: Geological Society of America Special Paper 227, p. 13–50.

Berger, G. W., 1990, Effectiveness of natural zeroing of the thermoluminescence in sediments: Journal of Geophysical Research, v. 95, p. 12375–12397.

Berger, G., 1995, Progress in luminescence dating methods for Quaternary sediments, *in* Rutter, N. W., and Catto, N. R., eds., Dating methods for Quaternary deposits: Geological Association of Canada, p. 81–104.

Berger, G. W., Lockhart, R. A., and Kuo, J., 1987, Regression and error analysis applied to the dose-response curves in thermoluminescence dating: Nuclear Tracks and Radiation Measurements, v. 13, p. 177–184.

Blair, T. C., and McPherson, J. G., 1994, Alluvial fans and their natural distinction from rivers based on morphology, hydraulic processes, sedimentary processes, and facies assemblages: Journal of Sedimentary Research, v. 64, p. 450–489.

Burbank, D. W., 1992, Causes of recent Himalayan uplift deduced from deposited patterns in the Ganges Basin: Nature, v. 357, p. 680–683.

Burchfiel, B. C., and Royden, L. H., 1991, Tectonics of Asia 50 years after the death of Emile Argand: Eclogae Geologicae Helvetiae, v. 84, p. 599–629.

Burchfiel, B. C., Chen, Z., Liu, Y., and Royden, L. H., 1995, Tectonics of the Longmen Shan and adjacent regions: International Geology Review, v. 37, p. 661–735.

Chen, S. F., Wilson, C. J. L., Deng, Q. D., Zhao, X. L., and Luo, Z. L., 1994, Active faulting and block movement associated with large earthquakes in the Min Shan and Longmen mountains, northeastern Tibetan Plateau: Journal of Geophysical Research, v. 99, p. 24025–24038.

Chen, Z., Burchfiel, B. C., Liu, Y., King, R. W., Royden, L. H., Tang, W., Wang, E., Zhao, J., and Zhang, X., 2000, GPS measurements from eastern Tibet and their implications for India/Eurasia intracontinental deformation: Journal of Geophysical Research (in press).

Cobbold, P. R., and Davy, P., 1988, Indentation tectonics in nature and experiment: 2. Central Asia: University of Uppsala Geological Institute Bulletin 14, p. 143–162.

Coward, M. P., Kidd, W. S. F., Pan, Y., Shackelton, R. M., and Zhang, H., 1988, The structure of the 1985 Tibet Geotraverse, Lhasa to Golmud, *in* Chang, C., Shackleton, R. M., Dewey, J. F., and Yin, J., eds., The geological evolution of Tibet: Royal Society of London Philosophical Transactions, p. 307–336.

Dewey, J. F., and Burke, K. C. A., 1973, Tibetan, Variscan and Precambrian basement reactivation: Products of a continental collision: Journal of Geology, v. 81, p. 683–692.

Editorial Board, State Seismological Bureau, 1989, Lithospheric dynamics atlas of China: Beijing, China Cartographic Publishing House, p. 23.

England, P., and Houseman, G., 1986, Finite strain calculations of continental deformation: 2. Comparison with the India-Asia collision zone: Journal of Geophysical Research, v. 91, p. 3664–3676.

England, P., and Molnar, P., 1990a, Surface uplift, uplift of rocks, and exhumation of rocks: Geology, v. 18, p. 1173–1177.

England, P., and Molnar, P., 1990b, Right-lateral shear and rotation as the explanation for strike-slip faulting in eastern Tibet: Nature, v. 344, p. 140–142.

Fielding, E. J., Isacks, B. L., Barazangi, M., and Duncan, C., 1994, How flat is Tibet?: Geology, v. 22, p. 163–167.

Han, W., and Xia, D., 1980, The Songpan-Pingwu earthquakes and the movement of the Sichuan-Qinghai block (in Chinese): Earthquake Science Research, v. 1, p. 39–48.

Harrison, T. M., Copeland, P., Kidd, W. S. F., and Yin, A., 1992, Raising Tibet: Science, v. 255, p. 1663–1670.

Huntley, D. J., and Clague, J. J., 1996, Optical dating of tsunami-laid sands: Quaternary Research, v. 46, p. 127–140.

Huntley, D. J., and Wintle, A. G., 1981, The use of alpha scintillation counting for measuring Th-230 and Pa-231 contents of ocean sediments: Canadian Journal of Earth Sciences, v. 18, p. 419–432.

Huntley, D. J., Berger, G. W., and Bowman, S. G. E., 1988, Thermoluminescence responses to alpha and beta irradiations, and age determinations when the high-dose response is non-linear: Radiation Effects, v. 105, p. 279–284.

Imbrie, J., Hays, J. D., Martinson, D. G., McIntyre, A., Mix, A. C., Morley, J. J., Pisias, N. G., Prell, W. G., and Shackleton, N. J., 1984, The orbital theory of Pleistocene climate: Support from a revised chronology of the marine delta ^{18}O record, *in* Berger, A. L., Imbrie, J., Hays, J., Kukla, G., and Saltzman, B., eds., Milankovitch and climate, Part 1: Boston, Reidel Publishing Company, p. 169–305.

Jin, Y., McNutt, M. K., and Zhu, Y., 1994, Evidence from gravity and topography data for folding of Tibet: Nature, v. 371, p. 669–674.

Jones, L. M., Han, W., Hauksson, E., Jin, A., Zhang, Y., and Luo, Z., 1984, Focal mechanisms of the Songpan earthquakes of August 1976 in Sichuan, China: Journal of Geophysical Research, v. 89, p. 7697–7707.

King, R. W., Shen, F., Burchfiel, B. C., Royden, L. H., Wang, E., Chen, Z., Liu, Y., Zhang, X., Zhao, J., and Li, Y., 1997, Geodetic measurement of crustal motion in southwest China: Geology, v. 25, p. 179–182.

Kirby, E., Reiners, P., Farley, K., Krol, M., Liu, Y., Chen, Z., and Tang, W., 1999, Late Cenozoic uplift and landscape evolution of the eastern margin of the Tibetan Plateau: Inferences from $^{40/39}$Ar and U-Th-He thermochronology: Geological Society of America Abstracts with Programs, v. 31, no. 7, p. A129.

Kooi, H., and Beaumont, C., 1994, Escarpment evolution on high-elevation rifted margins: Insights derived from a surface processes model that combines diffusion, advection, and reaction: Journal of Geophysical Research, v. 99, p. 12191–12209.

Kukla, G., 1987, Loess stratigraphy in China: Quaternary Science Reviews, v. 6, p. 191–219.

Lyon-Caen, H., and Molnar, P., 1983, Constraints on the structure of the Himalaya from an analysis of gravity anomalies and a flexural model of the lithosphere: Journal of Geophysical Research, v. 88, p. 8171–8191.

Masek, J. G., Isacks, B. L., and Fielding, E. J., 1994a, Rift flank uplift in Tibet: Evidence for a viscous lower crust: Tectonics, v. 13, p. 659–667.

Masek, J. G., Isacks, B. L., Gubbels, T. L., and Fielding, E. J., 1994b, Erosion and tectonics at the margins of continental plateaus: Journal of Geophysical Research, v. 99, p. 13941–13956.

Ministry of Geology and Mineral Resources, People's Republic of China, 1991, Regional geology of Sichuan Province: Beijing, Geological Publishing House, Geological Memoirs, ser. 1, no. 23, 728 p.

Molnar, P., 1988, A review of geophysical constraints on the deep structure of the Tibetan Plateau, the Himalaya and the Karakoram, and their tectonic implications, *in* Chang, C., Shackleton, R. M., Dewey, J. F., and Yin, J., eds., The geological evolution of Tibet: Royal Society of London Philosophical Transactions, p. 33–88.

Molnar, P., and England, P., 1990, Late Cenozoic uplift of mountain ranges and global climate change: Chicken or egg?: Nature, v. 346, p. 29–34.

Molnar, P., and Tapponnier, P., 1975, Cenozoic tectonics of Asia: Effects of a continental collision: Science, v. 189, p. 419–426.

Montgomery, D. R., 1994, Valley incision and the uplift of mountain peaks: Journal of Geophysical Research, v. 99, p. 13913–13921.

Nelson, K. D., Zhao, W., Brown, L. D., Kuo, J., Che, J., Liu, X., Klemperer, S. L., Makovsky, Y., Meissner, R., Mechie, J., Kind, R., Wenzel, F., Ni, J., Nabelek, J., Leshou, C., Tan, H., Wei, W., Jones, A. G., Booker, J., Unsworth, M., Kidd, W. S. F., Hauck, M., Alsdorf, D., Ross, A., Cogan, M., Wu, C., Sandvol, E., and Edwards, M., 1996, Partially molten middle crust beneath southern Tibet: Synthesis of project INDEPTH results: Science, v. 274, p. 1684–1688.

Ollerhead, J., Huntley, D. J., and Berger, G. W., 1994, Luminescence dating of the Buctouche Spit, New Brunswick: Canadian Journal of Earth Sciences, v. 31, p. 523–531.

Olley, J. M., Murray, A., and Roberts, R., 1996, The effects of disequilibria in the uranium and thorium decay chains on burial dose rates in fluvial sediments: Quaternary Science Reviews, v. 15, p. 751–760.

Paola, C., and Mohrig, D., 1996, Paleohydraulics revisited: Paleoslope estimation in coarse-grained braided rivers: Basin Research, v. 8, p. 243–254.

Pazzaglia, F. J., Gardner, T. W., and Merritts, D. J., 1998, Bedrock fluvial incision and longitudinal profile development over geologic time scales determined by fluvial terraces, *in* Tinkler, K. J., and Wohl, E. E., eds., Rivers over rock: Fluvial processes in bedrock channels: American Geophysical Union Geophysical Monograph 107, p. 207–235.

Prescott, J. R., and Hutton, J. T., 1988, Cosmic ray and gamma ray dosimetry for TL and ESR: Nuclear Tracks and Radiation Measurements, v. 14, p. 223–227.

Prescott, J. R., and Robertson, G. B., 1997, Sediment dating by luminescence: A review: Radiation Measurements, v. 27, p. 893–922.

Ratschbacher, L., Frisch, W., Chen, C., and Pan, G., 1996, Cenozoic deformation, rotation, and stress patterns in eastern Tibet and western Sichuan, China, *in* Yin, A., and Harrison, T. M., eds., The tectonic evolution of Asia: Cambridge, Cambridge University Press, p. 227–249.

Royden, L. H., Burchfiel, B. C., King, R. W., Chen, Z., Shen, F., and Liu, Y., 1997, Surface deformation and lower crustal flow in Eastern Tibet: Science, v. 276, p. 788–790.

Stuiver, M., and Reimer, P. J., 1993, Extended ^{14}C database and revised CALIB radiocarbon age calibration program: Radiocarbon, v. 35, p. 215–230.

Tang, R., Wen, D., Huang, Z., Wu, X., Lin, W., Chen, G., and Wu, G., 1993, The Quaternary activity characteristics of several major active fault zones in the Songpan-Longmenshan region: Earthquake Research in China, v. 7, p. 341–350.

Tapponnier, P., Peltzer, G., Le Dain, A. Y., Armijo, R., and Cobbold, P., 1982, Propagating extrusion tectonics in Asia: New insight from simple experiments with plasticine: Geology, v. 10, p. 611–616.

Tucker, G. E., and Slingerland, R. L., 1994, Erosional dynamics, flexural isostasy, and long-lived escarpments: A numerical modeling study: Journal of Geophysical Research, v. 99, p. 12229–12243.

Turcotte, D., and Schubert, G., 1982, Geodynamics: Applications of continuum physics to geological problems: New York, John Wiley and Sons, 450 p.

Wintle, A. G., and Huntley, D. J., 1980, Thermoluminescence dating of ocean sediments: Canadian Journal of Earth Sciences, v. 17, p. 348–360.

Zhao, X., Deng, Q., and Chen, S., 1994, Tectonic geomorphology of the Min Shan uplift in western Sichuan, southwestern China: Seismology and Geology, v. 16, no. 4, p. 429–439 (in Chinese with English abstract).

MANUSCRIPT RECEIVED BY THE SOCIETY AUGUST 20, 1999
REVISED MANUSCRIPT RECEIVED NOVEMBER 23, 1999
MANUSCRIPT ACCEPTED DECEMBER 7, 1999

Printed in U.S.A.